Cell Reports

Report

Microglia enable mature perineuronal nets disassembly upon anesthetic ketamine exposure or 60-Hz light entrainment in the healthy brain

Graphical abstract

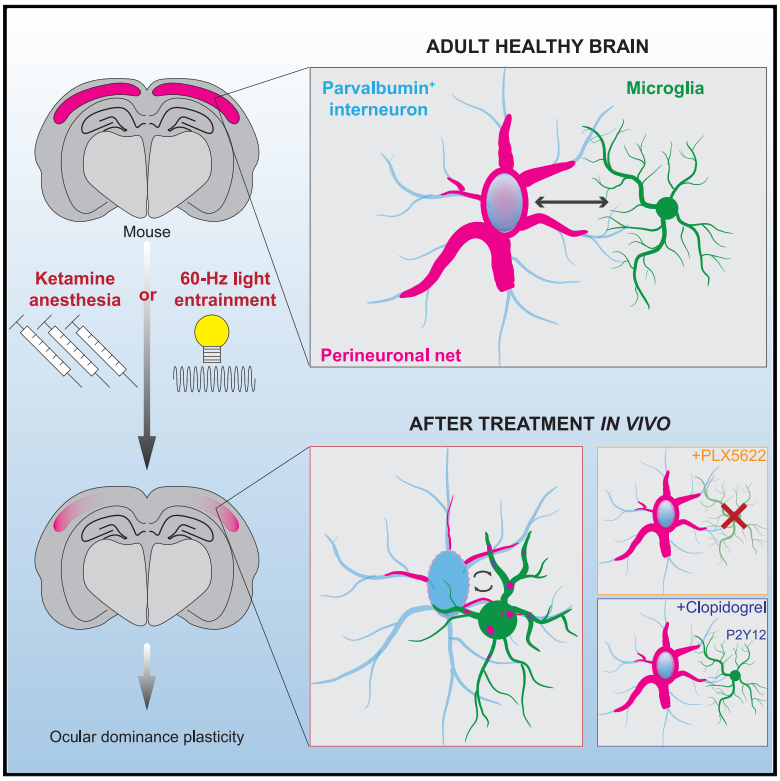

Highlights

- Repeated ketamine anesthesia induces perineuronal net loss
- PNN loss reinstates juvenile-like ocular dominance plasticity
- Microglia interact with parvalbumin neurons and remodel PNN
- 60-Hz light stimulation recapitulates ketamine-induced PNN loss

Authors

Alessandro Venturino, Rouven Schulz, Héctor De Jesús-Cortés, ..., Florianne E. Schoot Uiterkamp, Mark F. Bear, Sandra Siegert

Correspondence

sandra.siegert@ist.ac.at

In brief

Venturino et al. show that repeated ketamine anesthesia results in perineuronal net loss, which promotes juvenile-like, ocular-dominance plasticity in adult mice. Microglia are key players in the PNN disassembly, in which 60-Hz light entrainment reproduces that phenotype, providing an alternative, non-invasive strategy to remodel PNNs.

Venturino et al., 2021, Cell Reports *36*, 109313
July 6, 2021
https://doi.org/10.1016/j.celrep.2021.109313

CellPress

Cell Reports

CellPress
OPEN ACCESS

Report

Microglia enable mature perineuronal nets disassembly upon anesthetic ketamine exposure or 60-Hz light entrainment in the healthy brain

Alessandro Venturino,[1] Rouven Schulz,[1,3] Héctor De Jesús-Cortés,[2,3] Margaret E. Maes,[1] Bálint Nagy,[1] Francis Reilly-Andújar,[2] Gloria Colombo,[1] Ryan John A. Cubero,[1] Florianne E. Schoot Uiterkamp,[1] Mark F. Bear,[2] and Sandra Siegert[1,4,*]

[1]Institute of Science and Technology (IST) Austria, Am Campus 1, 3400 Klosterneuburg, Austria
[2]The Picower Institute for Learning and Memory, Department of Brain and Cognitive Sciences, Massachusetts Institute of Technology, Cambridge, MA 02139, USA
[3]These authors contributed equally
[4]Lead contact
*Correspondence: sandra.siegert@ist.ac.at
https://doi.org/10.1016/j.celrep.2021.109313

SUMMARY

Perineuronal nets (PNNs), components of the extracellular matrix, preferentially coat parvalbumin-positive interneurons and constrain critical-period plasticity in the adult cerebral cortex. Current strategies to remove PNN are long-lasting, invasive, and trigger neuropsychiatric symptoms. Here, we apply repeated anesthetic ketamine as a method with minimal behavioral effect. We find that this paradigm strongly reduces PNN coating in the healthy adult brain and promotes juvenile-like plasticity. Microglia are critically involved in PNN loss because they engage with parvalbumin-positive neurons in their defined cortical layer. We identify external 60-Hz light-flickering entrainment to recapitulate microglia-mediated PNN removal. Importantly, 40-Hz frequency, which is known to remove amyloid plaques, does not induce PNN loss, suggesting microglia might functionally tune to distinct brain frequencies. Thus, our 60-Hz light-entrainment strategy provides an alternative form of PNN intervention in the healthy adult brain.

INTRODUCTION

Sensory processing is established through experience during the critical period of brain development (Hensch, 2005). The end of that phase coincides with increased inhibition from fast-spiking parvalbumin-positive (Pvalb$^+$) neurons and the formation of the perineuronal net (PNN), a defined extracellular matrix (ECM) compartment consisting of chondroitin sulfate proteoglycans and various ECM and cell-adhesion molecules (Ueno et al., 2017a, 2018b). Approximately 80% of Pvalb$^+$ neurons in the primary somatosensory cortex are coated with PNN (Härtig et al., 1992; Ueno et al., 2018b; Wen et al., 2018). PNN sterically restricts synapse formation and receptor mobility and, thus, prevents adaptation of juvenile plasticity in adulthood (Celio and Blümcke, 1994; Frischknecht and Gundelfinger, 2012; Kuhlman et al., 2013; Lensjø et al., 2017; Pizzorusso et al., 2002). Disruptive environmental interferences during this sensitive period can cause long-lasting circuit impairment resulting in neurological disorders, such as loss of visual acuity (Fong et al., 2016). Enzymatic digestion of the ECM with intracerebral application of chondroitinase ABC can reinstate juvenile-like plasticity in the adult cortex, but the enzyme uncontrollably degrades the ECM for several weeks and is not suitable for therapeutic interventions (Hensch, 2005; Pizzorusso et al., 2002). An alternative approach surfaced in the form of the rapidly acting, dissociative drug ketamine, which preferentially acts on NMDA receptors of cortical inhibitory neurons (Brown et al., 2011; Kaplan et al., 2016; Li and Vlisides, 2016; Picard et al., 2019). Recent studies in rats suggested that repeated exposure of low dosage of ketamine mildly reduces PNN coverage (Kaushik et al., 2020; Matuszko et al., 2017). At the same time, that dosage regime provokes schizophrenia-like phenotypes, limiting its therapeutic use. We decided to circumvent that constraint by applying ketamine at an anesthetic dosage. Ketamine complies with the principles of general anesthesia, which requires a drug-inducible, fully-reversible change of consciousness and cognition (Brown et al., 2011). Mice exposed to repeated anesthetic ketamine showed only minimal effects in their well-being and behavior (Hohlbaum et al., 2018). Furthermore, the application of ketamine at anesthetic dosage achieves the maximum pharmacological response with a consistent phenotypic readout across animals, avoiding the confounding effects of ketamine dosage, frequency, and time interval. This allowed us to address the underlying cellular mechanism involved in PNN reduction, which provides the fundaments to find alternative, non-invasive strategies to modify PNN in the healthy adult brain.

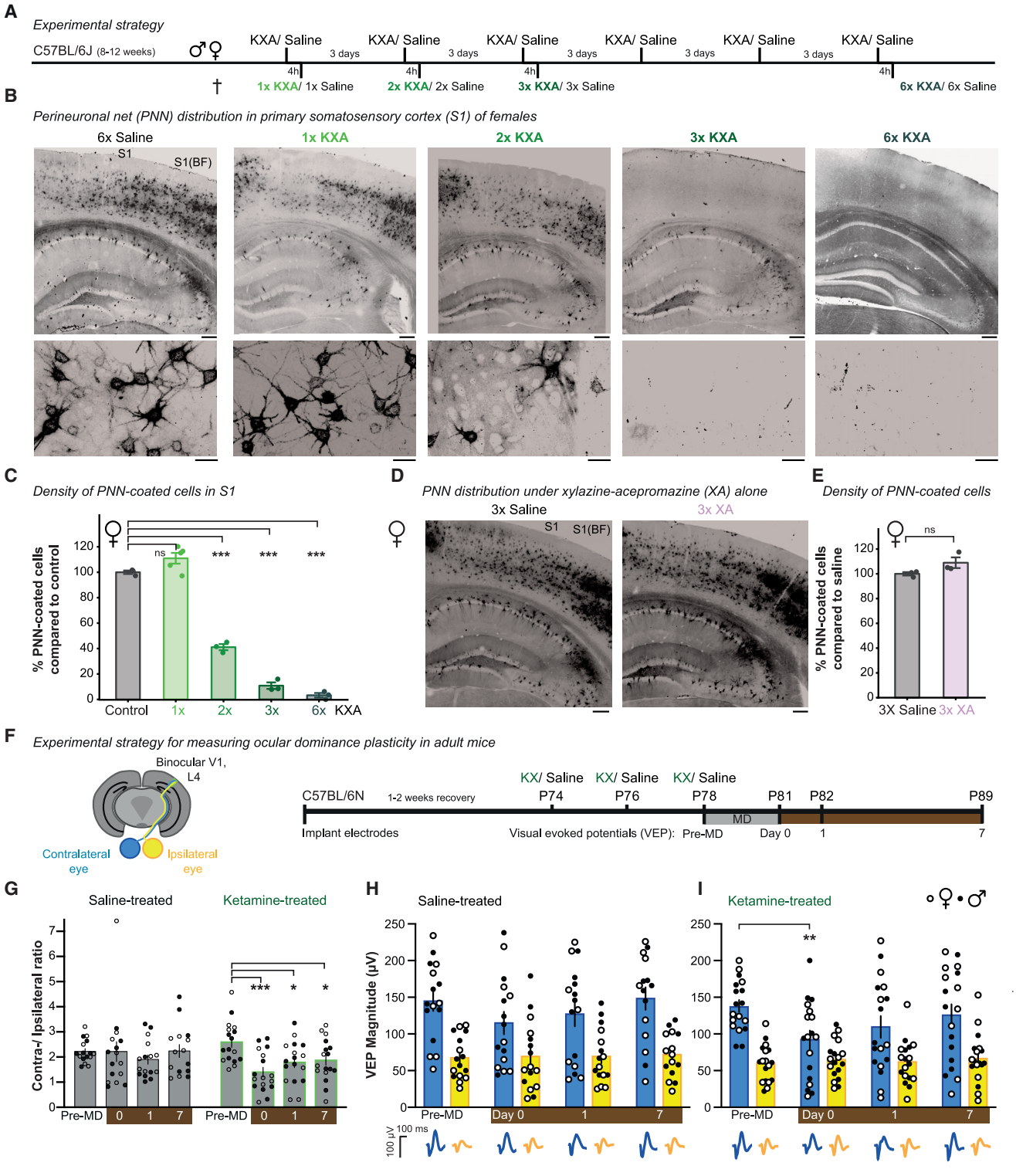

Figure 1. PNN gradually declines with repeated ketamine and reinstates juvenile-like plasticity

(A) Experimental timeline. KXA, ketamine-xylazine-acepromazine.

(B) *Wisteria floribunda* agglutinin (WFA)-labeled, female, coronal brain sections after 6× saline or 1× , 2× , 3× , or 6× KXA. Scale bar: 200 μm, zoom-in (S1): 20 μm. S1 (BF), somatosensory 1, barrel field.

(C) Percentage of change in mean PNN-coated cells ± SEM in S1. Linear regression model: $p_{♀} < 0.0001$ with selected post hoc comparisons.

(legend continued on next page)

Here, we show that repeated ketamine exposure at anesthetic dosage results in massive PNN loss in various cortical brain regions and is sufficient to promote juvenile-like plasticity. We identified microglia, the brain-resident immune cells (Kettenmann et al., 2011), to be critically involved in this process because they engaged with Pvalb$^+$ neurons in a layer-specific manner and subsequently remodeled the PNN coating. Because ketamine exposure influences the gamma frequency (Ahnaou et al., 2017; Castro-Zaballa et al., 2019; Pinault, 2008) and microglia are capable of removing extracellular amyloid-plaque depositions upon stimulation in the gamma range (Iaccarino et al., 2016), we entrained the visual cortex with either low- or high-light-flickering frequencies. At 60 Hz, we recapitulated the same microglia action toward PNN as seen under ketamine. Importantly, this only occurred at 60 Hz and not at 8 or 40 Hz, suggesting an alternative, non-invasive strategy to reduce PNN coverage in the healthy adult cortex.

RESULTS

Repeated ketamine exposure results in PNN loss

To establish the consequences of ketamine exposure on PNNs, we subjected adult C57BL/6J animals to single or repeated ketamine anesthesia at 3-day intervals and collected the brains 4 h after one, two, three, or six injections (Figure 1A). Because ketamine at this dosage induces muscle rigidity, we combined it with xylazine and the phenothiazine tranquilizer acepromazine (KXA). The PNN was stained with *Wisteria floribunda* agglutinin (WFA), which selectively binds to the *N*-acetyl-galactosamine group of the chondroitin sulfate proteoglycans of the PNN (Härtig et al., 1992) and has the highest density in layer 4 in the mouse somatosensory cortex (Ueno et al., 2018b; Wen et al., 2018). We confirmed that WFA is enriched in various brain regions (Figure S1A) and preferentially surrounds cortical Pvalb$^+$ neurons in layer 4 (Figure S1B). Strikingly with increased ketamine repetitions, coronal overview images showed substantial PNN loss in the primary somatosensory (S1) cortex (Figures 1B, S1C). To quantify the PNN loss, we took higher-magnification tile images, covering layers 3–5 and counted the number of WFA-stained cells in the S1 region. We confirmed the gradual decrease in the number of PNN-coated cells as predicted from the overview images (Figures 1C and S1D). This effect was not observed with the same number of repeated saline injections (Figures S2A and S2B) or xylazine-acepromazine (XA) injections (Figures 1D, 1E, S1E, and S1F), indicating that the effect is due to ketamine. Both sexes were similarly affected by ketamine (Figures 1B–1E, S1C–S1F, and S2C), excluding a long-term, sex-specific difference, as previously proposed (Carrier and Kabbaj, 2013; Thelen et al., 2016).

Excitotoxic cell death induced by ketamine could be an alternative cause for the PNN loss (Hauser et al., 2017; Schobel et al., 2013). Thus, we stained for caspase-3 and counted the number of Pvalb$^+$ neurons 4 h after the last injection of the 6× KXA treatment in S1. We did not observe caspase-3-positive cells (Figures S2D and S2E) or any changes in Pvalb$^+$ neuron density (Figure S2F). To further confirm PNN remodeling, we performed immunostaining for hyaluronic acid binding protein (HABP), a major ECM component and part of the PNN (Ueno et al., 2018a). HABP colocalizes with WFA-coated cells in the deeper cortical layers of S1 (Ueno et al., 2018a). After 3× KXA, HABP staining was evenly distributed throughout cortical layers 3–5 compared with 3× saline, and the number of HABP-coated cells was reduced to levels comparable to WFA-coated cells, whereas the overall relative mean fluorescence intensity remained unaltered (Figures S2G–S2I). Taken together, our data demonstrate that repeated ketamine exposure at an anesthetic dosage reduces the number of PNN-coated cells in the cortex.

Ketamine-mediated PNN loss promotes juvenile-like plasticity in adult mice

Next, we were interested in determining whether PNN removal would reinstate juvenile-like plasticity in the adult brain, using the well-established ocular dominance (OD) plasticity paradigm in the primary visual cortex (V1) (Frenkel and Bear, 2004; Sawtell et al., 2003; Ye and Miao, 2013). Similar to S1, we found that 3× KXA results in PNN loss in V1 (Figures S3A and S3B) and occurs independent of XA (Figure S3C), mouse strain background (Figures S3D and S3E), or sex (Figure S3F).

In general, P40 marks the cutoff for OD shifts after short-term (<5 days) monocular deprivation (MD) (Gordon and Stryker, 1996; Sato and Stryker, 2008). Because PNN was still significantly reduced 3 days after recovery from 3× KXA (Figures S3A and S3B), we tested whether 3 days of MD, initiated after the last KX dose, was sufficient to induce OD plasticity in adult animals. Thus, we measured visually evoked potentials (VEPs) before and after MD in binocular layer 4 of V1 (Figure 1F). In normally reared mice, the deprived contralateral eye-evoked response was two to three times greater than the non-deprived, ipsilateral, eye-evoked response, yielding a contralateral (C) to ipsilateral (I) eye ratio of ~2.5. In saline-treated animals, neither the contralateral-to-ipsilateral (C/I) VEP ratio nor the absolute amplitude of VEPs evoked by the two eyes was affected by 3-day MD, as expected in adult mice (Figures 1G and 1H). Although ketamine treatment did not significantly affect the C/I ratio or VEP magnitudes at baseline, it did render the visual cortex vulnerable to brief MD. After 3-day MD, the C/I ratio was shifted significantly to favor the non-deprived ipsilateral eye (Figure 1G), which was accounted for

(D) WFA-labeled female brain sections after 3× saline or XA. Scale bar: 200 μm.
(E) Percentage of change in mean PNN-coated cells ± SEM in S1. Two-sample t test: $p_{♀} = 0.1193$.
(F) Experimental timeline. L4, cortical layer 4. MD, monocular deprivation.
(G) Mean contra-/ipsilateral eye ratios per animal ± SEM. Two-way repeated-measure ANOVA: $p = 0.0341$.
(H and I) Mean monocular VEP magnitudes ± SEM with representative traces for (H) saline (contralateral, Friedman's test, $p = 0.1550$, ipsilateral, one-way ANOVA, $p = 0.9102$), or (I) ketamine-treated mice (contralateral, Friedman's, $p = 0.0097$ with selected post hoc comparisons; ipsilateral, Friedman's $p = 0.7546$).
Each dot in (C) and (E) represents one animal (3–5 animals per condition with the exception of the control bar in (C), which shows the mean value of all controls (see also Figure S2B).
*$p < 0.05$, **$p < 0.01$, ***$p < 0.001$, $^{ns}p > 0.05$.

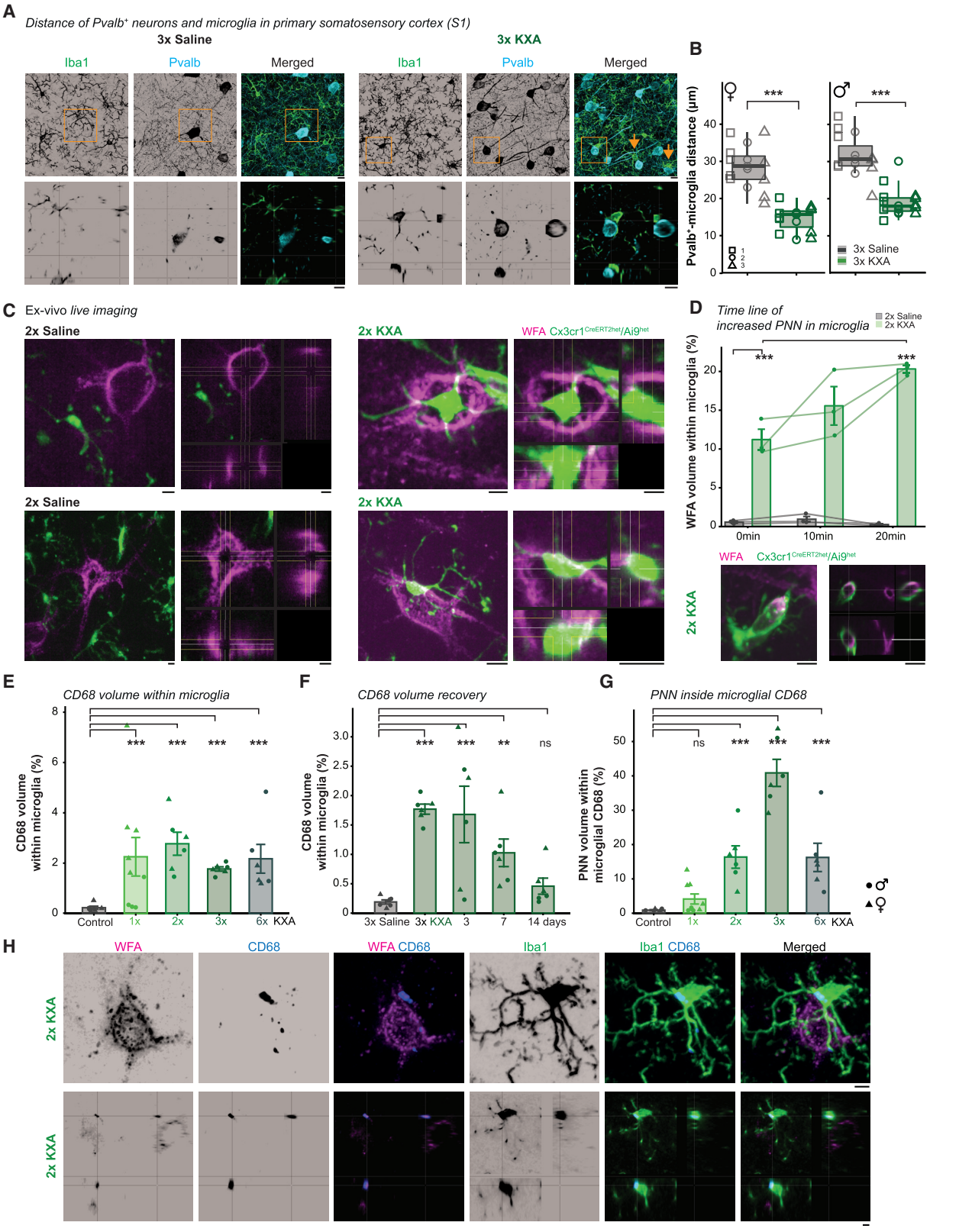

(legend on next page)

exclusively by a decrease in the amplitude of responses through the deprived contralateral eye (Figure 1I). Quantitatively and qualitatively, this OD shift is comparable to what is observed in young mice at ~P30 (Frenkel and Bear, 2004). In addition, we confirmed the OD shift with a significantly reduced C/I VEP ratio that persisted for at least a week after MD (Figure 1G). Our results show that PNN loss via repeated ketamine exposure promotes juvenile-like OD plasticity in adult animals.

Microglia interact with Pvalb$^+$ neurons and remodel PNN

Fast-spiking Pvalb$^+$ neurons as well as PNN coating are a critical component for establishing OD plasticity during the visual critical period (Hensch, 2005; Ueno et al., 2017b, 2018b; Wen et al., 2018). Because a recent study indicated a role for microglia in that context (Sipe et al., 2016), we investigated whether an interaction between Pvalb$^+$ neurons and microglia exists. The immunostaining for parvalbumin and the microglial marker Iba1 did not result in an obvious phenotype under 3× saline (Figure 2A). In contrast, after 3× KXA, microglia showed a close interaction with Pvalb$^+$ neurons (Figure 2B). Next, we investigated the expression of matrix metalloproteinase 9 (MMP-9), which has been shown to have a critical role in juvenile and adult OD plasticity and is released in a neuronal-activity-dependent manner (Dziembowska et al., 2012; Fawcett et al., 2019; Kaczmarek, 2016; Murase et al., 2017; Pielecka-Fortuna et al., 2015; Reinhard et al., 2015; Tewari et al., 2018). Pvalb$^+$ neurons and microglia localized in cortical layers 3–5 significantly increased MMP-9 upon 3× KXA (Figures S4A and S4B), whereas microglia in cortical layer 1 and astrocytes lacked that effect (Figures S4C and S4D). We also quantified the percentage of Pvalb$^+$ neurons and microglia containing MMP-9 and found in both cases a 3-fold increase after 3× KXA (Figures S4A and S4B).

To support microglial interaction with WFA-coated structures, we performed *ex vivo* live imaging from coronal brain slices in the S1 of Cx3cr1-^{CreERT2het}/Ai9^{het} animals prepared 2 h after the second KXA or saline injection and stained for WFA fluorescein isothiocyanate (FITC). We chose to image after 2× KXA because the number of PNN-coated cells was significantly decreased, yet enough WFA-stained cells remained to allow reliable detection (Figure 1C). Under 2× KXA, microglia were in constant contact with the soma of WFA-labeled cells and accumulated WFA-fragments to WFA-containing compartments within their cell soma over the course of 20 min (Figures 2C and 2D). Compared with saline-treated animals, the WFA accumulation was significantly greater under KXA. Consequently, the WFA-staining became unevenly distributed around the neuronal cell body. In contrast, the WFA-coated structures remained condensed after saline treatment, and the microglia were more ramified and acted in a surveying mode. Next, we analyzed the expression of the endosomal-lysosomal marker CD68, which increases when microglia transition from a surveillant to a reactive state (Bauer et al., 1994). In control, saline-injected animals, CD68 levels were unaltered (Figure S5A), whereas KXA exposure led to elevated CD68 levels that stayed upregulated (Figures 2E and S5B). CD68 gradually started to decline only 3 days after the last injection of 3× KXA (Figures 2F, S5C, and S5D). To substantiate whether CD68 contained a WFA signal, we quantified the volume of the WFA signal inside microglial CD68. The WFA volume increased with the amount of KXA exposure, reaching the peak at 3× KXA (Figures 2G, 2H, S6A, and S6B). Interestingly, the level of WFA-containing CD68 dropped precipitously 3 days after the last KXA injection (Figures S6C and S6D) in both S1 and V1 suggesting that, without further KXA stimulation, microglia gradually revert to the surveillant modus, permitting the recovery of the PNN coating (Figures S3A and S3B).

Finally, to confirm that microglia are a critical component for PNN removal, we depleted microglia by feeding mice the colony-stimulating factor 1 receptor (CSF1R) antagonist PLX5622 for 1.5 weeks, before and during 3× KXA treatment (Figure 3A). In contrast to PLX3397, PLX5622 has faster kinetics in depleting microglia and greater specificity to the CSF1R, with a potential caveat that it affects long-lived tissue macrophages in the body (Liu et al., 2019). The PLX5622 treatment caused an approximately 80% reduction in the microglial population (Figures S7A and S7B), which was sufficient to prevent a decrease in the number of PNN-coated cells after 3× KXA treatment (Figures 3B and 3C). The WFA staining maintained a condensed, network-like structure and did not dissolve in fragments, as noticed under repeated KXA (Figures 2H and S6A). Overall, these data strongly support the idea that microglia presence is necessary for PNN removal upon ketamine exposure and that microglia are actively involved.

Microglia-mediated PNN remodeling is inducible with 60-Hz light stimulation

In vivo electrophysiological recordings of various species have shown that ketamine alters brain oscillatory dynamics without

Figure 2. Microglia interact with PNN-coated neurons upon repeated ketamine stimulation

(A) Immunostaining for Iba1 (green) and parvalbumin (Pvalb, cyan) after 3× saline or KXA in primary somatosensory cortex S1. Zoom-in, single-plane orthogonal projection. Arrow, microglia in close distance to Pvalb$^+$ neurons. Scale bar: 10 μm.

(B) Minimal Pvalb$^+$ neuron-microglia median distance in micrometers after treatment. Each condition included three animals as indicated, five microglia per animal. Linear regression model with animal ID as the random effect: $p_{♀} < 0.0001$, $p_{♂} < 0.0001$.

(C and D) *Ex vivo* live imaging of brain slices of Cx3Cr1$^{CreERT2\ het}$/Ai9^{het} mice dissected 2 h after 2× KXA. Snapshots of microglia (green) and WFA (magenta) with orthogonal side projection. Scale bar: 10 μm. (D) Time course of mean WFA volume within microglia percentage ± SEM after treatment. Linear regression model: $p < 0.0001$ with selected post hoc comparisons.

(E and F) Mean percentage CD68 volume within microglia ± SEM after (E) saline or KXA or (F) 3× KXA recovery. See also Figures S5A and S5B. Linear regression model: (E) $p < 0.0001$, (F) $p < 0.0001$ with selected post hoc comparisons.

(G) Mean percentage of PNN volume within microglial CD68 ± SEM upon treatment. Linear regression model: $p < 0.0001$ with selected post hoc comparisons. Each dot represents one animal (3–5 animals per condition with exception of the control bar in (E) and (G), which shows the mean value of all controls. See also Figures S5A and S6B).

(H) Immunostaining for PNN (WFA, magenta), endosomal-lysosomal marker CD68 (blue), and microglia (Iba1, green) after 2× KXA. Bottom: single-plane orthogonal projections. Scale bar: 5 μm. $^{**}p < 0.01$, $^{***}p < 0.001$, $^{ns}p > 0.05$.

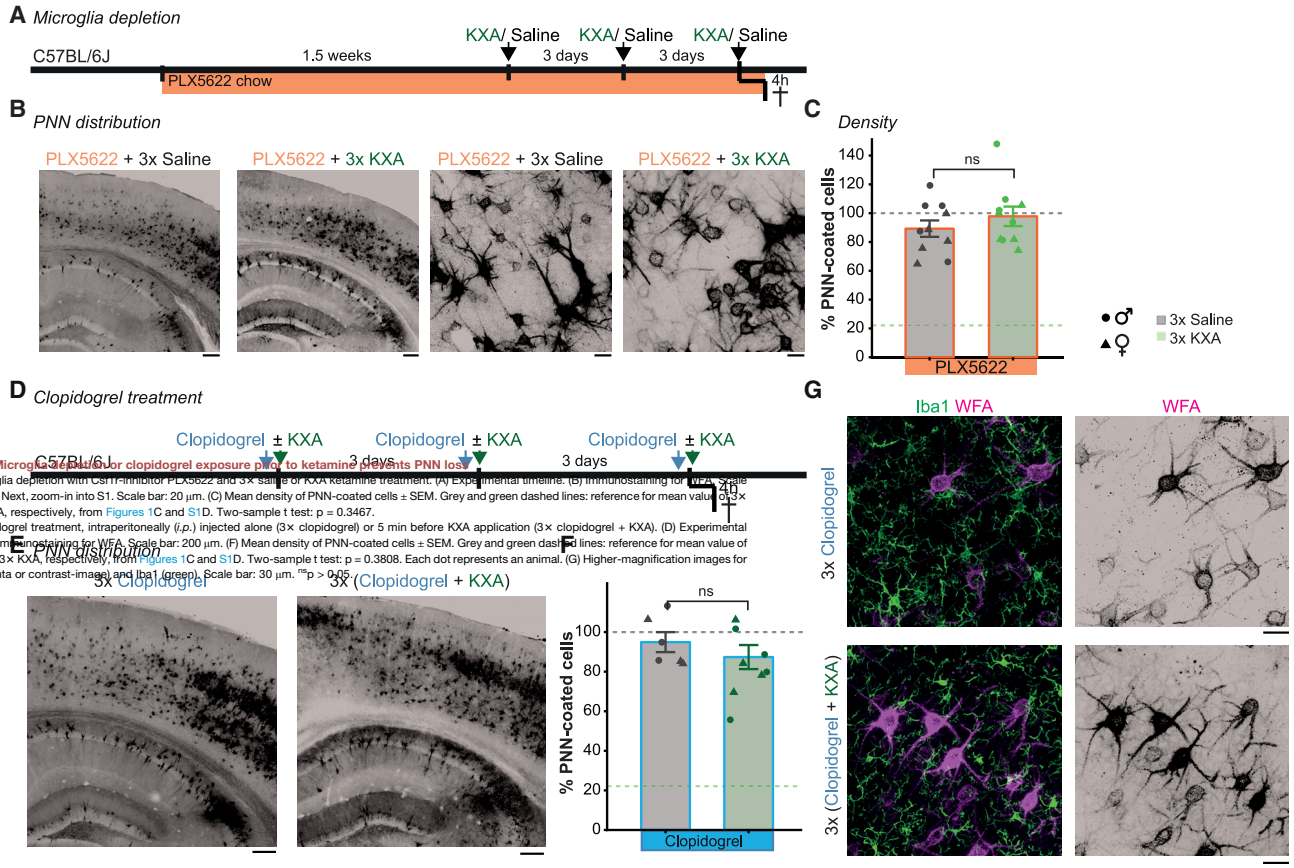

Figure 3. Microglia depletion or clopidogrel exposure prior to ketamine prevents PNN loss

(A–C) Microglia depletion with CSF1-inhibitor PLX5622 and 3× saline or KXA ketamine treatment. (A) Experimental timeline. (B) Immunostaining for PNN. Scale bar: 200 μm. Next, zoom-in into S1. Scale bar: 20 μm. (C) Mean density of PNN-coated cells ± SEM. Grey and green dashed lines: reference for mean value of 3× saline or KXA, respectively, from Figures 1C and S1D. Two-sample t test: p = 0.3467.

(D–G) Clopidogrel treatment, intraperitoneally (*i.p.*) injected alone (3× clopidogrel) or 5 min before KXA application (3× clopidogrel + KXA). (D) Experimental timeline. (E) Immunostaining for WFA. Scale bar: 200 μm. (F) Mean density of PNN-coated cells ± SEM. Grey and green dashed lines: reference for mean value of 3× saline or 3× KXA, respectively, from Figures 1C and S1D. Two-sample t test: p = 0.3808. Each dot represents an animal. (G) Higher-magnification images for WFA (magenta or contrast-images) and Iba1 (green). Scale bar: 30 μm. $^{ns}p > 0.05$.

inducing epileptic-seizure bursts (Ahnaou et al., 2017; Castro-Zaballa et al., 2019; Pinault, 2008). Pvalb$^+$ neurons contribute to cortical gamma oscillation (Cardin et al., 2009; Sohal et al., 2009). Because we identified enhanced interaction of microglia with Pvalb$^+$ neurons after KXA treatment (Figure 2B), we sought to determine whether the effect of microglia-mediated PNN remodeling was triggered by neuronal activity.

Microglia are known to sense changes in ATP/ADP levels from action potentials or injuries (Davalos et al., 2005; Fields, 2011; Nimmerjahn et al., 2005) via various purinergic receptors, such as P2Y12, which, upon activation, induces a chemotactic response (Haynes et al., 2006; Sipe et al., 2016). Therefore, we determined whether impaired P2Y12-mediated detection of neuronal activity prevents microglia from removing PNN. After confirming that P2Y12 surface expression remained unaltered upon ketamine exposure (Figure S7C), we injected clopidogrel to block one of the ATP/ADP detection mechanisms before KXA treatment (Figure 3D). Systemic application of clopidogrel has been shown to disrupt P2Y12 signaling in resident microglia, and the active metabolite has blood-brain-barrier permeability (Herbert et al., 1993; Sipe et al., 2016). Indeed, we found that this treatment regime prevented ketamine-mediated loss of PNN-coated cells (Figures 3E and 3F). Furthermore, the overall WFA-stained structure remained intact (Figure 3G), suggesting that changes in neuronal activity could be one of the driving forces of the microglial response.

Microglia respond to low gamma oscillation and can be stimulated with external light entrainment to remove extracellular amyloid plaque dispositions (Bolmont et al., 2008; Iaccarino et al., 2016). Based on ketamine's effect in the gamma oscillations, ranging from 25 to 100 Hz (Ahnaou et al., 2017; Castro-Zaballa et al., 2019; Pinault, 2008), we hypothesized that light entrainment at that frequency range might trigger microglia-mediated PNN remodeling. Thus, we selected 40 Hz and 60 Hz as representatives for the lower or higher gamma frequency, respectively. As controls, we applied constant bright light for the same amount of time or a theta (8 Hz) flickering frequency (Figure 4A). The power spectrum of the local field potentials across

CellPress
OPEN ACCESS

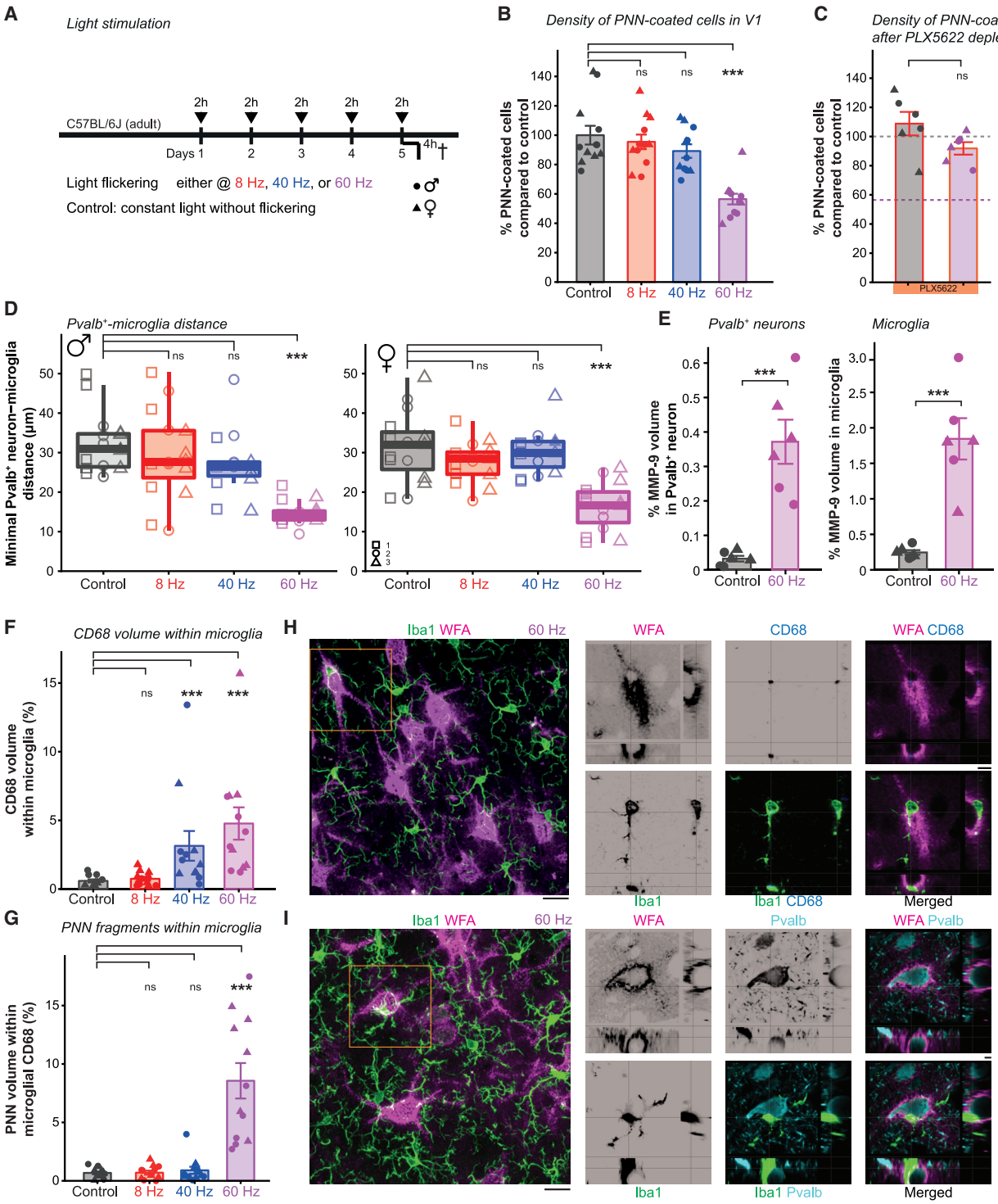

Figure 4. 60-Hz light flickering recapitulates microglia response observed under repeated ketamine exposure

Light stimulation either with constant light (black) or light-flickering frequencies at 8 Hz (red), 40 Hz (blue), or 60 Hz (purple) in V1.

(A) Experimental timeline.

(B and C) Mean density of WFA-coated cells in percentage ± SEM (B) Linear regression model with selected post hoc comparisons: $p < 0.0001$. (C) After microglia depletion. Two-sample t test: $p = 0.0926$. Grey and purple dashed lines: reference for mean value of constant light or 60 Hz from (B), respectively.

(D) Median minimal parvalbumin $(Pvalb)^+$ neuron-microglia distance. Each condition included three animals, as indicated, five microglia per animal. Linear regression model: $p_{♂} < 0.0001$, $p_{♀} < 0.0001$ with selected post hoc comparisons.

(legend continued on next page)

the V1 cortical region verified that our selected light entrainment frequency reached the V1 (Figure S7D) and confirmed previous studies (Fries et al., 2007; Gray et al., 1989; Herrmann, 2001; Rager and Singer, 1998). Strikingly, we found that selective 60-Hz flickering reduced the number of PNN-coated cells in the V1, whereas the other frequencies or constant light did not cause a reduction (Figures 4B and S7E). This effect was not observed when microglia were depleted 1.5 weeks before the 60-Hz light-flickering stimulation (Figures 4C and S7F). Similar to repeated ketamine exposure, the distance between Pvalb$^+$ neurons and microglia only decreased upon 60-Hz light flickering (Figures 4D and S8A), and MMP-9 levels increased in both Pvalb$^+$ neurons and microglia (Figures 4E, S8B, and S8C). Importantly, although microglia showed a significant increase in CD68 volume after 40 and 60 Hz gamma light-flickering (Figure 4F), we only observed an enrichment of WFA fragments within microglia upon 60-Hz stimulation (Figures 4G and 4H). On several occasions, microglia cell bodies sat on top of WFA-coated cell-body-like structures and enabled PNN dismantling (Figures 4H and 4I). In addition, we observed increased CD68 enrichment at the perforation site, which was not found at the other frequencies (Figures 4H and S9). These data provide an alternative, non-invasive strategy to remodel PNN under defined, externally driven brain-activity entrainment.

DISCUSSION

Ketamine induces microglia-mediated PNN remodeling

Throughout development, microglia have been shown to affect synapse formation and circuit connectivity (Kettenmann et al., 2013; Paolicelli et al., 2011; Schafer et al., 2012; Tremblay et al., 2010). During the visual critical period, monocular deprivation results in reactive microglia, which interact with synaptic elements and affect ocular-dominance plasticity (Sipe et al., 2016). This effect is usually only observed before the PNN formation reaches a plateau at around P42 (Ye and Miao, 2013). From then onward, multiple studies have demonstrated that short-term monocular deprivation can only cause a shift in ocular-dominance plasticity upon enzymatic digestion of the ECM (Frenkel and Bear, 2004; Lensjø et al., 2017; Pizzorusso et al., 2002). Therefore, we were surprised that repeated anesthetic ketamine exposure alone resulted in a reduced coverage of PNN-coated cells (Figures 1B and S1C) associated with ocular-dominance plasticity after brief periods of monocular deprivation, resembling what is observed during the juvenile period (Figures 1F–1I). This shift was dependent on visual deprivation because the VEP recordings after 3× KXA and before monocular deprivation did not affect the contra-to-ipsilateral ratio.

Furthermore, our results provide extensive evidence that ketamine exposure initiates microglia to remodel PNN. Recent studies suggested that microglia are capable of removing PNN in various neurological disorders and altering ECM in the adult hippocampus (Crapser et al., 2020; Nguyen et al., 2020). A similar effect was described for repeated exposure to a low ketamine dosage, which is a common model to induce schizophrenia-like phenotypes in rats (Kaushik et al., 2020; Matuszko et al., 2017). Here, we decided to take advantage of ketamine's compliance to the principles of general anesthesia and that repeated exposure only caused mild behavioral changes (Hohlbaum et al., 2018). Moreover, the systematically delivered ketamine at an anesthetic dosage achieved the maximum pharmacological response comparable across animals without running into conflicts, such as dosage or injection frequency. Our ketamine dosage was 100 mg/Kg, which can only be provided in combination with xylazine. Because we excluded xylazine-acepromazine as an effector (Figures 1D and S1E), our results support a ketamine dosage-dependent response in PNN reduction, extending the repertoire of known dose-dependent ketamine actions (Lavender et al., 2020) with the caveat that anesthetic ketamine dosage has a plethora of effects, which is not straightforward to dissect.

Commonly, the PNN is composed of multiple extracellular molecules, such as chondroitin sulfate proteoglycans (CSPGs), hyaluronic acid, and linker proteins. To label the PNN, we used the well-defined marker WFA, which selectively binds to the terminal ends of the *N*-acetyl-galactosamine groups of CSPGs (Fawcett et al., 2019; Härtig et al., 1992; Ueno et al., 2017a, 2018b; Wen et al., 2018). We confirmed the high specificity of this staining in cortical layers 3–5 by demonstrating the selective WFA-coating around Pvalb$^+$ neurons (Figures S1A and S1B). Moreover, we identified that the distance of microglia to Pvalb$^+$ neurons was reduced under ketamine exposure (Figure 2B) and that microglia actively interacted with, and contained, WFA-coated structures (Figures 2C and 2D). A common misconception is that "reactive" microglia must change into an amoeboid morphology containing multiple phagocytic cups (Wolf et al., 2017). However, this strong reaction is usually only observed in injury and disease environments, in which substantial cell death occurs. We did not observe this phenotype with repeated ketamine exposure (Figure S2D). Instead, we found with our *ex vivo* live imaging that microglia frequently screen the WFA-labeled structures, even in the control conditions, suggesting a constant exchange between microglia and PNN-coated neurons. One potential modulator of this interaction could be MMP-9 because it has been suggested to be involved in PNN degradation (Kelly et al., 2015; Murase et al., 2017). To that end, we observed increased MMP-9 level in both Pvalb$^+$ neurons and microglia upon ketamine exposure (Figure S4). However, the role of MMP-9 is not fully understood because it can target the CSPG core protein directly (Hadler-Olsen et al., 2011; Malla et al., 2008; Pielecka-Fortuna et al., 2015; Spolidoro et al., 2012; Tewari et al., 2018; de Vivo et al., 2013; Wen et al.,

(E) Mean percentage of change in MMP-9 volume ± SEM within each cell type. Two-sample t test: Pvalb$^+$-neurons, $p < 0.0001$. Microglia, $p < 0.0001$.
(F) Mean percentage of CD68 volume ± SEM within microglia. Linear regression model: $p < 0.0001$ with selected post hoc comparisons.
(G) Mean percentage ± SEM of WFA volume within microglial CD68. Linear regression model: $p < 0.0001$ with selected post hoc comparisons.
(H and I) Immunostained PNN (WFA, magenta), microglia (Iba1, green), endosomal-lysosomal marker CD68 (blue, H), and Pvalb (cyan, I) after 60-Hz light-flickering stimulation. Scale bar: 20 μm. Frame indicates zoom-in and single-plane orthogonal projections. Scale bar: 7 μm (H) and 4 μm (I). $^{***}p < 0.001$, $^{ns}p > 0.05$. With the exception of (D), each dot represents an animal.

2018; Winberg et al., 2003) or indirectly, and it can act as a signaling molecule to modulate neurotrophins, other ECM-regulatory components, cell-adhesion molecules, or synaptic receptors (Beroun et al., 2019; Dityatev et al., 2010; Dziembowska et al., 2012; Kaczmarek, 2016). In addition to MMP-9, other alternative ECM peptidases could also be involved in the PNN loss. Nevertheless, microglia's action under ketamine led us to reveal that they are capable of remodeling the PNN upon externally introduced neuronal activity entrainment. This provided a foundation to identify alternative strategies to alter PNN because repeated ketamine exposure can lead to adverse side effects, including schizophrenia-like phenotypes and response to general anesthesia (Brown et al., 2011).

Gamma entrainment at 60-Hz stimulates microglia

In addition to PNN preventing receptor mobility and synapse formation, the PNN composition fosters a negatively charged local environment supporting the fast-spiking properties of cortical Pvalb$^+$ neurons (Tewari et al., 2018) that modulate gamma brain network activity (Cardin et al., 2009; Sohal et al., 2009). Ketamine application transiently alters brain dynamics mainly in the 30–80-Hz gamma-frequency range (Ahnaou et al., 2017; Castro-Zaballa et al., 2019; Pinault, 2008), suggesting that neuronal activity might trigger microglia to remodel PNN. Loss of the 40-Hz gamma frequency in a model of Alzheimer's disease has been indicated to cause extracellular amyloid-plaque aggregations. This study entrained the cortical circuits with externally applied light-flickering at 40 Hz and observed microglia phagocytosing amyloid plaques, reducing one of the hallmarks of the disease (Iaccarino et al., 2016). Multiple studies have shown that external light entrainment reaches and drives oscillation in the visual cortex (Fries et al., 2001; Gray et al., 1989; Herrmann, 2001; Rager and Singer, 1998), which we confirmed (Figure S7D). We also prove that microglia reacted to 40-Hz entrainment with increased CD68 expression (Figure 4F). However, only with 60-Hz entrainment did we replicate the ketamine-mediated effects, including WFA staining inside microglial CD68 (Figure 4G), MMP-9 upregulation in both Pvalb$^+$ neurons and microglia (Figure 4E), and an overall reduced number of PNN-coated cells (Figure 4B). If we depleted microglia before the 60-Hz stimulation, the number of PNN-coated cells did not change (Figure 4C) suggesting that microglia show a selective response toward PNN in the healthy, adult cortex.

In summary, we demonstrate that repeated ketamine exposure at an anesthetic dosage reduces PNN levels and promotes juvenile-like plasticity. This strong, microglia-dependent effect provided the fundaments to identify and confirm 60-Hz light entrainment as an alternative, non-invasive strategy to modify PNN levels without the potential side effects of repetitive ketamine exposure.

Limitations of study

Microglia prove to be a critical cellular component for PNN loss upon repeated stimulation; however, the amount of WFA material inside microglia does not directly reflect the substantial PNN loss. We suspect that MMP-9-mediated enzymatic degradation of the PNN before engulfment was responsible for that discrepancy, yet information on the molecular mechanism for MMP-9 involvement in either Pvalb$^+$ neuron-microglial communication and/or PNN disassembly remains limited. Further studies are required to determine cell type and cortical-layer-specific MMP-9 expression patterns and whether MMP-9 is released and extracellularly active. Additional mechanistic insights could be obtained through a screen for alternative endopeptidases and ECM components. The latter would overcome one limitation of WFA, which also labels disaggregated CSPG in the ECM. Despite the orthogonal projections to confirm WFA inside microglial CD68, we cannot fully exclude that additional ECM components remain intact and are omitted from microglial uptake. Lastly, the anesthetic dosage of ketamine might limit mechanistic insights because of many brain-region-specific effects that are likely not exclusive to Pvalb$^+$ neurons. Then again, when we entrained the visual cortex with 60-Hz light flickering, we were able to reproduce the ketamine-induced observation, suggesting that alteration in neuronal activity is a driving force, which is a focus of ongoing investigation.

STAR★METHODS

Detailed methods are provided in the online version of this paper and include the following:

- KEY RESOURCES TABLE
- RESOURCE AVAILABILITY
  - Lead contact
  - Materials availability
  - Data and code availability
- EXPERIMENTAL MODEL AND SUBJECT DETAILS
  - Animals
- METHOD DETAILS
  - Drug application
  - Ketamine-xylazine-acepromazine (KXA)
  - Ketamine-xylazine (KX)
  - Xylazine-acepromazine (XA)
  - Control
  - Repeated KXA
  - PLX5622
  - Clopidogrel
  - Tamoxifen administration
  - Light flicker stimulation
  - Tissue preparation
  - Immunohistochemistry
  - Confocal microscopy
  - Image analysis
  - Adult ocular dominance plasticity
  - Live imaging of WFA/microglia
  - In-vivo electrophysiology
- QUANTIFICATION AND STATISTICAL ANALYSIS
  - Combined controls
  - Perineuronal net density per mm^3
  - Sex differences

SUPPLEMENTAL INFORMATION

Supplemental information can be found online at https://doi.org/10.1016/j.celrep.2021.109313.

ACKNOWLEDGMENTS

We thank the scientific service units at IST Austria, especially the IST bioimaging facility, the preclinical facility, and, specifically, Michael Schunn and Sonja Haslinger for excellent support; Plexxikon for the PLX food; the Csicsvari group for advice and equipment for *in vivo* recording; Jürgen Siegert for the light-entrainment design; Marco Benevento, Soledad Gonzalo Cogno, Pat King, and all Siegert group members for constant feedback on the project and manuscript; Lorena Pantano (PILM Bioinformatics Core) for assisting with sample-size determination for OD plasticity experiments; and Ana Morello from MIT for technical assistance with VEPs recordings. This research was supported by a DOC Fellowship from the Austrian Academy of Sciences at the Institute of Science and Technology Austria to R.S., from the European Union Horizon 2020 research and innovation program under the Marie Skłodowska-Curie Actions program (grants 665385 to G.C.; 754411 to R.J.A.C.), the European Research Council (grant 715571 to S.S.), and the National Eye Institute of the National Institutes of Health under award numbers R01EY029245 (to M.F.B.) and R01EY023037 (diversity supplement to H.D.J-C.).

AUTHOR CONTRIBUTIONS

Conceptualization, A.V. and S.S.; investigation, validation, and methodology, A.V., M.E.M., G.C., B.N., F.E.S.U, and S.S.; formal analysis and software, R.S. and R.J.A.C; writing – original draft, A.V., H.D.J.-C., M.F.B., and S.S.; writing – review & editing, A.V., M.E.M., B.N., H.D.J.-C., and S.S.; supervision and funding acquisition, S.S.; for OD plasticity, conceptualization, A.V., H.D.J.-C., M.F.B., and S.S.; investigation and formal analysis, H.D.J.-C. and F.R.-A.; supervision and funding acquisition, M.F.B.

DECLARATION OF INTERESTS

The authors declare no competing interests. A.V. and S.S. disclose an international patent application (PCT/EP2020/079365).

INCLUSION AND DIVERSITY

We worked to ensure sex balance in the selection of non-human subjects.

Received: August 20, 2020
Revised: November 20, 2020
Accepted: June 4, 2021
Published: July 6, 2021

REFERENCES

Ahnaou, A., Huysmans, H., Biermans, R., Manyakov, N.V., and Drinkenburg, W.H.I.M. (2017). Ketamine: differential neurophysiological dynamics in functional networks in the rat brain. Transl. Psychiatry *7*, e1237.

Bates, D., Mächler, M., Bolker, B., and Walker, S. (2015). Fitting linear mixed-effects models using lme4. arXiv, arXiv:1406.5823v1.

Bauer, J., Sminia, T., Wouterlood, F.G., and Dijkstra, C.D. (1994). Phagocytic activity of macrophages and microglial cells during the course of acute and chronic relapsing experimental autoimmune encephalomyelitis. J. Neurosci. Res. *38*, 365–375.

Beroun, A., Mitra, S., Michaluk, P., Pijet, B., Stefaniuk, M., and Kaczmarek, L. (2019). MMPs in learning and memory and neuropsychiatric disorders. Cell. Mol. Life Sci. *76*, 3207–3228.

Bolmont, T., Haiss, F., Eicke, D., Radde, R., Mathis, C.A., Klunk, W.E., Kohsaka, S., Jucker, M., and Calhoun, M.E. (2008). Dynamics of the microglial/amyloid interaction indicate a role in plaque maintenance. J. Neurosci. *28*, 4283–4292.

Brown, E.N., Purdon, P.L., and Van Dort, C.J. (2011). General anesthesia and altered states of arousal: a systems neuroscience analysis. Annu. Rev. Neurosci. *34*, 601–628.

Cardin, J.A., Carlén, M., Meletis, K., Knoblich, U., Zhang, F., Deisseroth, K., Tsai, L.H., and Moore, C.I. (2009). Driving fast-spiking cells induces gamma rhythm and controls sensory responses. Nature *459*, 663–667.

Carrier, N., and Kabbaj, M. (2013). Sex differences in the antidepressant-like effects of ketamine. Neuropharmacology *70*, 27–34.

Castro-Zaballa, S., Cavelli, M.L., Gonzalez, J., Nardi, A.E., Machado, S., Scorza, C., and Torterolo, P. (2019). EEG 40 Hz coherence decreases in REM sleep and ketamine model of psychosis. Front. Psychiatry *9*, 766.

Celio, M.R., and Blümcke, I. (1994). Perineuronal nets—a specialized form of extracellular matrix in the adult nervous system. Brain Res. Brain Res. Rev. *19*, 128–145.

Crapser, J.D., Spangenberg, E.E., Barahona, R.A., Arreola, M.A., Hohsfield, L.A., and Green, K.N. (2020). Microglia facilitate loss of perineuronal nets in the Alzheimer's disease brain. EBioMedicine *58*, 102919.

Dagher, N.N., Najafi, A.R., Kayala, K.M.N., Elmore, M.R.P., White, T.E., Medeiros, R., West, B.L., and Green, K.N. (2015). Colony-stimulating factor 1 receptor inhibition prevents microglial plaque association and improves cognition in 3xTg-AD mice. J. Neuroinflammation *12*, 139.

Davalos, D., Grutzendler, J., Yang, G., Kim, J.V., Zuo, Y., Jung, S., Littman, D.R., Dustin, M.L., and Gan, W.B. (2005). ATP mediates rapid microglial response to local brain injury *in vivo*. Nat. Neurosci. *8*, 752–758.

de Vivo, L., Landi, S., Panniello, M., Baroncelli, L., Chierzi, S., Mariotti, L., Spolidoro, M., Pizzorusso, T., Maffei, L., and Ratto, G.M. (2013). Extracellular matrix inhibits structural and functional plasticity of dendritic spines in the adult visual cortex. Nat. Commun. *4*, 1484.

Dityatev, A., Schachner, M., and Sonderegger, P. (2010). The dual role of the extracellular matrix in synaptic plasticity and homeostasis. Nat. Rev. Neurosci. *11*, 735–746.

Dragulescu, A.A. (2014). Read, write, format Excel 2007 (xlsx) files (R Foundation for Statistical Computing).

Dziembowska, M., Milek, J., Janusz, A., Rejmak, E., Romanowska, E., Gorkiewicz, T., Tiron, A., Bramham, C.R., and Kaczmarek, L. (2012). Activity-dependent local translation of matrix metalloproteinase-9. J. Neurosci. *32*, 14538–14547.

Fawcett, J.W., Oohashi, T., and Pizzorusso, T. (2019). The roles of perineuronal nets and the perinodal extracellular matrix in neuronal function. Nat. Rev. Neurosci. *20*, 451–465.

Fields, R.D. (2011). Nonsynaptic and nonvesicular ATP release from neurons and relevance to neuron-glia signaling. Semin. Cell Dev. Biol. *22*, 214–219.

Fong, M.F., Mitchell, D.E., Duffy, K.R., and Bear, M.F. (2016). Rapid recovery from the effects of early monocular deprivation is enabled by temporary inactivation of the retinas. Proc. Natl. Acad. Sci. USA *113*, 14139–14144.

Frenkel, M.Y., and Bear, M.F. (2004). How monocular deprivation shifts ocular dominance in visual cortex of young mice. Neuron *44*, 917–923.

Fries, P., Reynolds, J.H., Rorie, A.E., and Desimone, R. (2001). Modulation of oscillatory neuronal synchronization by selective visual attention. Science *291*, 1560–1563.

Fries, P., Nikolić, D., and Singer, W. (2007). The gamma cycle. Trends Neurosci. *30*, 309–316.

Frischknecht, R., and Gundelfinger, E.D. (2012). The brain's extracellular matrix and its role in synaptic plasticity. Adv. Exp. Med. Biol. *970*, 153–171.

Gordon, J.A., and Stryker, M.P. (1996). Experience-dependent plasticity of binocular responses in the primary visual cortex of the mouse. J. Neurosci. *16*, 3274–3286.

Gray, C.M., König, P., Engel, A.K., and Singer, W. (1989). Oscillatory responses in cat visual cortex exhibit inter-columnar synchronization which reflects global stimulus properties. Nature *338*, 334–337.

Hadler-Olsen, E., Fadnes, B., Sylte, I., Uhlin-Hansen, L., and Winberg, J.O. (2011). Regulation of matrix metalloproteinase activity in health and disease. FEBS J. *278*, 28–45.

Härtig, W., Brauer, K., and Brückner, G. (1992). Wisteria floribunda agglutinin-labelled nets surround parvalbumin-containing neurons. Neuroreport *3*, 869–872.

Hauser, M.J., Isbrandt, D., and Roeper, J. (2017). Disturbances of novel object exploration and recognition in a chronic ketamine mouse model of schizophrenia. Behav. Brain Res. *332*, 316–326.

Haynes, S.E., Hollopeter, G., Yang, G., Kurpius, D., Dailey, M.E., Gan, W.B., and Julius, D. (2006). The P2Y12 receptor regulates microglial activation by extracellular nucleotides. Nat. Neurosci. *9*, 1512–1519.

Hensch, T.K. (2005). Critical period plasticity in local cortical circuits. Nat. Rev. Neurosci. *6*, 877–888.

Herbert, J.M., Frehel, D., Vallee, E., Kieffer, G., Gouy, D., Berger, Y., Necciari, J., Defreyn, G., and Maffrand, J.P. (1993). Clopidogrel, a novel antiplatelet and antithrombotic agent. Cardiovasc. Drug Rev. *11*, 180–198.

Herrmann, C.S. (2001). Human EEG responses to 1-100 Hz flicker: resonance phenomena in visual cortex and their potential correlation to cognitive phenomena. Exp. Brain Res. *137*, 346–353.

Hohlbaum, K., Bert, B., Dietze, S., Palme, R., Fink, H., and Thöne-Reineke, C. (2018). Impact of repeated anesthesia with ketamine and xylazine on the well-being of C57BL/6JRj mice. PLoS ONE *13*, e0203559.

Hothorn, T., Bretz, F., and Westfall, P. (2008). Simultaneous inference in general parametric models. Biom. J. *50*, 346–363.

Iaccarino, H.F., Singer, A.C., Martorell, A.J., Rudenko, A., Gao, F., Gillingham, T.Z., Mathys, H., Seo, J., Kritskiy, O., Abdurrob, F., et al. (2016). Gamma frequency entrainment attenuates amyloid load and modifies microglia. Nature *540*, 230–235.

Kaczmarek, L. (2016). Mmp-9 in control of synaptic plasticity: a subjective account. Opera Med. Physiol. *2*, 103–111.

Kaplan, E.S., Cooke, S.F., Komorowski, R.W., Chubykin, A.A., Thomazeau, A., Khibnik, L.A., Gavornik, J.P., and Bear, M.F. (2016). Contrasting roles for parvalbumin-expressing inhibitory neurons in two forms of adult visual cortical plasticity. eLife *5*, e11450.

Kaushik, R., Lipachev, N., Matuszko, G., Kochneva, A., Dvoeglazova, A., Becker, A., Paveliev, M., and Dityatev, A. (2020). Fine structure analysis of perineuronal nets in the ketamine model of schizophrenia. Eur. J. Neurosci.

Kelly, E.A., Russo, A.S., Jackson, C.D., Lamantia, C.E.L., and Majewska, A.K. (2015). Proteolytic regulation of synaptic plasticity in the mouse primary visual cortex: analysis of matrix metalloproteinase 9 deficient mice. Front. Cell. Neurosci. *9*, 369.

Kettenmann, H., Hanisch, U.K., Noda, M., and Verkhratsky, A. (2011). Physiology of microglia. Physiol. Rev. *91*, 461–553.

Kettenmann, H., Kirchhoff, F., and Verkhratsky, A. (2013). Microglia: new roles for the synaptic stripper. Neuron *77*, 10–18.

Kuhlman, S.J., Olivas, N.D., Tring, E., Ikrar, T., Xu, X., and Trachtenberg, J.T. (2013). A disinhibitory microcircuit initiates critical-period plasticity in the visual cortex. Nature *501*, 543–546.

Lavender, E., Hirasawa-Fujita, M., and Domino, E.F. (2020). Ketamine's dose related multiple mechanisms of actions: Dissociative anesthetic to rapid antidepressant. Behav. Brain Res. *390*, 112631.

Lensjø, K.K., Lepperød, M.E., Dick, G., Hafting, T., and Fyhn, M. (2017). Removal of perineuronal nets unlocks juvenile plasticity through network mechanisms of decreased inhibition and increased gamma activity. J. Neurosci. *37*, 1269–1283.

Li, L., and Vlisides, P.E. (2016). Ketamine: 50 years of modulating the mind. Front. Hum. Neurosci. *10*, 612.

Liu, Y., Given, K.S., Dickson, E.L., Owens, G.P., Macklin, W.B., and Bennett, J.L. (2019). Concentration-dependent effects of CSF1R inhibitors on oligodendrocyte progenitor cells ex vivo and in vivo. Exp. Neurol. *318*, 32–41.

Malla, N., Berg, E., Uhlin-Hansen, L., and Winberg, J.O. (2008). Interaction of pro-matrix metalloproteinase-9/proteoglycan heteromer with gelatin and collagen. J. Biol. Chem. *283*, 13652–13665.

Matuszko, G., Curreli, S., Kaushik, R., Becker, A., and Dityatev, A. (2017). Extracellular matrix alterations in the ketamine model of schizophrenia. Neuroscience *350*, 13–22.

Murase, S., Lantz, C.L., and Quinlan, E.M. (2017). Light reintroduction after dark exposure reactivates plasticity in adults via perisynaptic activation of MMP-9. Elife *6*, e27345.

Nguyen, P.T., Dorman, L.C., Pan, S., Vainchtein, I.D., Han, R.T., Nakao-Inoue, H., Taloma, S.E., Barron, J.J., Molofsky, A.B., Kheirbek, M.A., and Molofsky, A.V. (2020). Microglial remodeling of the extracellular matrix promotes synapse plasticity. Cell *182*, 388–403.e15.

Nimmerjahn, A., Kirchhoff, F., and Helmchen, F. (2005). Resting microglial cells are highly dynamic surveillants of brain parenchyma in vivo. Science *308*, 1314–1318.

Paolicelli, R.C., Bolasco, G., Pagani, F., Maggi, L., Scianni, M., Panzanelli, P., Giustetto, M., Ferreira, T.A., Guiducci, E., Dumas, L., et al. (2011). Synaptic pruning by microglia is necessary for normal brain development. Science *333*, 1456–1458.

Parkhurst, C.N., Yang, G., Ninan, I., Savas, J.N., Yates, J.R., 3rd, Lafaille, J.J., Hempstead, B.L., Littman, D.R., and Gan, W.B. (2013). Microglia promote learning-dependent synapse formation through brain-derived neurotrophic factor. Cell *155*, 1596–1609.

Picard, N., Takesian, A.E., Fagiolini, M., and Hensch, T.K. (2019). NMDA 2A receptors in parvalbumin cells mediate sex-specific rapid ketamine response on cortical activity. Mol. Psychiatry *24*, 828–838.

Pielecka-Fortuna, J., Kalogeraki, E., Fortuna, M.G., and Löwel, S. (2015). Optimal level activity of matrix metalloproteinases is critical for adult visual plasticity in the healthy and stroke-affected brain. eLife *5*, e11290.

Pinault, D. (2008). N-methyl d-aspartate receptor antagonists ketamine and MK-801 induce wake-related aberrant λ oscillations in the rat neocortex. Biol. Psychiatry *63*, 730–735.

Pizzorusso, T., Medini, P., Berardi, N., Chierzi, S., Fawcett, J.W., and Maffei, L. (2002). Reactivation of ocular dominance plasticity in the adult visual cortex. Science *298*, 1248–1251.

Rager, G., and Singer, W. (1998). The response of cat visual cortex to flicker stimuli of variable frequency. Eur. J. Neurosci. *10*, 1856–1877.

Reinhard, S.M., Razak, K., and Ethell, I.M. (2015). A delicate balance: role of MMP-9 in brain development and pathophysiology of neurodevelopmental disorders. Front. Cell. Neurosci. *9*, 280.

Sato, M., and Stryker, M.P. (2008). Distinctive features of adult ocular dominance plasticity. J. Neurosci. *28*, 10278–10286.

Savi, P., Labouret, C., Delesque, N., Guette, F., Lupker, J., and Herbert, J.M. (2001). P2y(12), a new platelet ADP receptor, target of clopidogrel. Biochem. Biophys. Res. Commun. *283*, 379–383.

Sawtell, N.B., Frenkel, M.Y., Philpot, B.D., Nakazawa, K., Tonegawa, S., and Bear, M.F. (2003). NMDA receptor-dependent ocular dominance plasticity in adult visual cortex. Neuron *38*, 977–985.

Schafer, D.P., Lehrman, E.K., Kautzman, A.G., Koyama, R., Mardinly, A.R., Yamasaki, R., Ransohoff, R.M., Greenberg, M.E., Barres, B.A., and Stevens, B. (2012). Microglia sculpt postnatal neural circuits in an activity and complement-dependent manner. Neuron *74*, 691–705.

Schobel, S.A., Chaudhury, N.H., Khan, U.A., Paniagua, B., Styner, M.A., Asllani, I., Inbar, B.P., Corcoran, C.M., Lieberman, J.A., Moore, H., and Small, S.A. (2013). Imaging patients with psychosis and a mouse model establishes a spreading pattern of hippocampal dysfunction and implicates glutamate as a driver. Neuron *78*, 81–93.

Sipe, G.O., Lowery, R.L., Tremblay, M.È., Kelly, E.A., Lamantia, C.E., and Majewska, A.K. (2016). Microglial P2Y12 is necessary for synaptic plasticity in mouse visual cortex. Nat. Commun. *7*, 10905.

Sohal, V.S., Zhang, F., Yizhar, O., and Deisseroth, K. (2009). Parvalbumin neurons and gamma rhythms enhance cortical circuit performance. Nature *459*, 698–702.

Spangenberg, E., Severson, P.L., Hohsfield, L.A., Crapser, J., Zhang, J., Burton, E.A., Zhang, Y., Spevak, W., Lin, J., Phan, N.Y., et al. (2019). Sustained

microglial depletion with CSF1R inhibitor impairs parenchymal plaque development in an Alzheimer's disease model. Nat. Commun. *10*, 3758.

Spolidoro, M., Putignano, E., Munafò, C., Maffei, L., and Pizzorusso, T. (2012). Inhibition of matrix metalloproteinases prevents the potentiation of nondeprived-eye responses after monocular deprivation in juvenile rats. Cereb. Cortex *22*, 725–734.

Tewari, B.P., Chaunsali, L., Campbell, S.L., Patel, D.C., Goode, A.E., and Sontheimer, H. (2018). Perineuronal nets decrease membrane capacitance of peritumoral fast spiking interneurons in a model of epilepsy. Nat. Commun. *9*, 4724.

Thelen, C., Sens, J., Mauch, J., Pandit, R., and Pitychoutis, P.M. (2016). Repeated ketamine treatment induces sex-specific behavioral and neurochemical effects in mice. Behav. Brain Res. *312*, 305–312.

Tremblay, M.Ě., Lowery, R.L., and Majewska, A.K. (2010). Microglial interactions with synapses are modulated by visual experience. PLoS Biol. *8*, e1000527.

Tsukamoto, A., Serizawa, K., Sato, R., Yamazaki, J., and Inomata, T. (2015). Vital signs monitoring during injectable andn inhalant anesthesia in mice. Exp. Anim. *64*, 57–64.

Ueno, H., Suemitsu, S., Murakami, S., Kitamura, N., Wani, K., Okamoto, M., Matsumoto, Y., and Ishihara, T. (2017a). Region-specific impairments in parvalbumin interneurons in social isolation-reared mice. Neuroscience *359*, 196–208.

Ueno, H., Suemitsu, S., Okamoto, M., Matsumoto, Y., and Ishihara, T. (2017b). Sensory experience-dependent formation of perineuronal nets and expression of Cat-315 immunoreactive components in the mouse somatosensory cortex. Neuroscience *355*, 161–174.

Ueno, H., Suemitsu, S., Murakami, S., Kitamura, N., Wani, K., Matsumoto, Y., Aoki, S., Okamoto, M., and Ishihara, T. (2018a). Hyaluronic acid is present on specific perineuronal nets in the mouse cerebral cortex. Brain Res. *1698*, 139–150.

Ueno, H., Suemitsu, S., Murakami, S., Kitamura, N., Wani, K., Matsumoto, Y., Okamoto, M., and Ishihara, T. (2018b). Layer-specific expression of extracellular matrix molecules in the mouse somatosensory and piriform cortices. IBRO Rep. *6*, 1–17.

Wen, T.H., Binder, D.K., Ethell, I.M., and Razak, K.A. (2018). The perineuronal 'safety' net? perineuronal net abnormalities in neurological disorders. Front. Mol. Neurosci. *11*, 270.

Wickham, H. (2016). ggplot2—Elegant Graphics for Data Analysis (Springer).

Winberg, J.O., Berg, E., Kolset, S.O., and Uhlin-Hansen, L. (2003). Calcium-induced activation and truncation of promatrix metalloproteinase-9 linked to the core protein of chondroitin sulfate proteoglycans. Eur. J. Biochem. *270*, 3996–4007.

Wolf, S.A., Boddeke, H.W.G.M., and Kettenmann, H. (2017). Microglia in physiology and disease. Annu. Rev. Physiol. *79*, 619–643.

Ye, Q., and Miao, Q.L. (2013). Experience-dependent development of perineuronal nets and chondroitin sulfate proteoglycan receptors in mouse visual cortex. Matrix Biol. *32*, 352–363.

Zhang, H., Lauver, D.A., Wang, H., Sun, D., Hollenberg, P.F., Chen, Y.E., Osawa, Y., and Eitzman, D.T. (2016). Significant improvement of antithrombotic responses to clopidogrel by use of a novel conjugate as revealed in an arterial model of thrombosiss. J. Pharmacol. Exp. Ther. *359*, 11–17.

Zhang, K., Fujita, Y., and Hashimoto, K. (2018). Lack of metabolism in (*R*)-ketamine's antidepressant actions in a chronic social defeat stress model. Sci. Rep. *8*, 4007.

STAR★METHODS

KEY RESOURCES TABLE

REAGENT or RESOURCE	SOURCE	IDENTIFIER
Antibodies		
rabbit α-Caspase 3	Cell Signaling	Cat#9661S, Lot 45; RRID:AB_2341188
rat α-CD68	AbD Serotec	Cat#MCA1957, clone FA-11, Lot 1807; RRID:AB_322219
goat α-Iba1	Abcam	Cat#ab5076, Lot FR3288145-1; RRID:AB_2224402
rabbit a-Iba1	GeneTex	Cat#GTX100042, Lot 41556; RRID:AB_1240434
rabbit α-MMP-9	Abcam	Cat#ab38898, Lot GR3204084-23; RRID:AB_776512
guinea pig α-parvalbumin	Synaptic Systems	Cat#195004, Lot 2505; RRID:AB_2156476
chicken α-parvalbumin	Novus Biologicals	Cat#NBP2-50036, Lot 72715; RRID:AB_2814697
rabbit α-P2y12	Sigma	Cat#HPA014518, Lot F119293; RRID:AB_2669027
chicken α-S100β	Synaptic Systems	Cat#287006, Lot 1-3; RRID:AB_2713986
Chemicals, peptides, and recombinant proteins		
Biotinylated Hyaluronan Binding protein	Amsbio	Cat#AMS.HKD-BC41, Lot SA
Wisteria floribunda lectin – fluorescein-labeled	Szabo-Scandic	Cat#VECFL-1351, Lot ZE0611
Wisteria floribunda lectin – biotinylated	Szabo-Scandic	Cat#VECB-1355, Lot ZE0424
Clopidogrel	Tocris	Cat#2490
Hoechst 33342	Thermo Fisher Scientific	Cat#H3570
Isoflurane	Zoetis	Cat#6089373
Ketamine	MSD Animal Health	Cat#A137A01
Xylazine	AniMedica	Cat#7630517
Acepromazine	VANA GmbH	Cat#18F211
PLX5622	Research diets	Cat#113512
Metamizol	Sanofi Aventis	Cat#Ay005
Meloxicam	Boehringer-Ingelheim	KPOEH3R
Experimental models: Organisms/strains		
Mouse: C57BL/6J	The Jackson Laboratories	Cat#000664
Mouse: B6.129P2(C)-Cx3cr1tm2.1(cre/ERT2)Jung/J	The Jackson Laboratories	Cat#020940
Mouse: B6;129S6-Gt(ROSA)26Sortm9	The Jackson Laboratories	Cat#007909
Mouse: C57BL/6N	The Jackson Laboratories	Cat#005304
Mouse: C57BL/6NCrl	Charles River Laboratories	Cat#027
Software and algorithms		
R	r-project.org	version 3.4.4
Fiji	https://imagej.net/Fiji	1.52e
Chronux	http://chronux.org	RRID: SCR_005547 (Version 2.12)
MATLAB R2019b	MathWorks	RRID: SCR_001622
Python	https://www.python.org/	RRID: SCR_008394 (Version 3.7)
MatPlotLib	https://matplotlib.org	RRID: SCR_008624 (Version 3.4.1)
Imaris	Bitplane Imaris	8.4.2

RESOURCE AVAILABILITY

Lead contact

Further information and requests for resources and reagents should be directed to and will be fulfilled by the lead contact, Sandra Siegert (sandra.siegert@ist.ac.at).

Materials availability
The study did not generate new unique reagents.

Data and code availability
This study did not generate any unique datasets or code.

EXPERIMENTAL MODEL AND SUBJECT DETAILS

Animals
If not otherwise indicated, adult mice (8-12 weeks) of both sexes were used. C57BL/6J (Cat#000664), C57BL/6N (Cat#005304), B6.129P2(C)-Cx3cr1tm2.1(cre/ERT2)Jung/J (Cat#020940, named here: Cx3Cr1^{CreERT2}) and B6;129S6-Gt(ROSA)26Sortm9(CAG-tdTomato)Hze/J (Cat#007909, named here: Ai9) were purchased from The Jackson Laboratories. Cx3Cr1^{CreERT2} were heterozygous. All mice were housed in the IST Austria Preclinical Facility with a 12 hour light-dark cycle, food and water provided *ad libitum*. All animal procedures are approved by the Bundesministerium für Wissenschaft, Forschung und Wirtschaft (bmwfw) Tierversuchsgesetz 2012 (TVG 2012), BGBI. I Nr. 114/2012, idF BGBI. I Nr. 31/2018 under the numbers 66.018/0005-WF/V/3b/2016, 66.018/0010-WF/V/3b/2017, 66.018/0025-WF/V/3b/2017, 66.018/0001_V/3b/2019, 2020-0.272.234.

Visually-evoked potential recordings were done in the lab of M.F.B. at MIT with adult C57BL/6NCrl animals of both sexes, which were purchased from Charles River Laboratories (Cat#027) and maintained at the MIT animal facility. Animals were housed with a 12 hour light-dark cycle, food and water provided *ad libitum* and in groups of 3 or more. We used 34 animals from 10 litters for the final dataset. All procedures were approved by the MIT Committee on Animal Care (CAC) and adhere to the guideline of the National Institute of Health (NIH).

METHOD DETAILS

Drug application
If not otherwise indicated, C57BL/6J mice were given intraperitoneal (*i.p.*) injections of drug or saline in the morning. Deep anesthesia was confirmed based on the following parameters: 1. Absence of the toe pinch reflex around 10 minutes after induction. 2. Decrease in the respiratory frequency. 3. No responses to noxious stimuli. 4. Flaccid paralysis. 5. Absence of whisker movement (Tsukamoto et al., 2015). To prevent corneal dehydration, eye ointment (Oleo Vital) was applied. During the procedure and recovery phase, animals were kept at 37°C.

Ketamine-xylazine-acepromazine (KXA)
Ketamine (100 mg/kg, MSD Animal Health, Cat #A137A01), xylazine (10 mg/kg, AniMedica, Cat#7630517) and acepromazine (3 mg/kg, VANA GmbH, Cat#18F211) were solubilized in physiological saline solution containing 0.9% (w/v) NaCl (Fresenius Kabi Austria, Cat#19MIA700). Solution was always freshly prepared to avoid pH fluctuations.

Ketamine-xylazine (KX)
For OD plasticity experiments (performed in the lab of M.F.B. at MIT), ketamine (Ketset, 100 mg/kg, Zoetis, Cat#1051) and xylazine (Pivetal/Anased, 10 mg/kg, Patterson Veterinary, Cat#04606-6750-02) were used at the same concentrations as described above. The protocol did not contain acepromazine because the most recent animal protocol did not contain the drug and acepromazine has no effect on PNN density in combination with xylazine (Figures 1D, 1E, S1E, S1F, and S3C).

Xylazine-acepromazine (XA)
Xylazine and acepromazine, without ketamine, at the same concentration as described in Ketamine-xylazine-acepromazine (KXA).

Control
Saline (*i.p.*) volume corresponding to KXA cocktail concentration was injected.

Repeated KXA
Animals were exposed either to 1 × , 2 × , 3 × , or 6 × KXA injections with 2-4 days between the treatments (Hohlbaum et al., 2018).

PLX5622
The animals received chow containing 1200 mg/kg PLX5622 (Research diets, #113512) 1.5 weeks before the first KXA injection, and were kept on that diet for the whole duration of the experiment (Dagher et al., 2015; Spangenberg et al., 2019).

Clopidogrel
Clopidogrel (Tocris, Cat#2490) was dissolved in dimethyl sulfoxide (DMSO, Sigma, Cat#D8418) and diluted 1:4 in phosphate buffer saline (PBS) before the injection. 50 mg/kg Clopidogrel were injected (*i.p.*) 5 minutes before KXA, which reaches peak plasma levels within 1 min of intravenous administration (Savi et al., 2001; Zhang et al., 2016).

Tamoxifen administration

Adult Cx3Cr1$^{CreERT2\ het}$/Ai9 ^{het} mice were injected intraperitoneally with 150 mg/kg tamoxifen (Sigma, Cat#T5648, Lot WXBD2299V, dissolved in corn oil, Sigma, Cat#MKCH1635) for three consecutive days. Mice were sacrificed for *ex-vivo* imaging at least four weeks after tamoxifen administration to ensure that the Ai9 reporter is only visible in resident microglia (Parkhurst et al., 2013).

Light flicker stimulation

The stimulation box consists of a black plastic box with a lid (OBI Tauro 62 Liters, 60 × 40 × 32 cm). A strip of light emitting diodes (LEDs, RS Components, Part. N. LSWW61210MIP20) was attached to the side walls of the box. The flicker frequency was set at 8, 40 or 60 Hz with a square wave current pattern generated using an Arduino system (Arduino UNO SMD). The frequency of flickering was verified using a photoresistor (5 mm GL5516 LDR Photo Resistance), controlled by an Arduino UNO, positioned 1 cm from the LED strip. Images for circuit diagram were generated with fritzing app (version 0.9.3b). 3.9 × 10^{18} photons/cm^2/s were generated in the center of the stimulation box.

Mice were transported from the holding room of the animal facility to the laboratory. Before the cage was put in the center of the stimulation box, 8 cm away from the LEDs, all nesting materials and tools were removed. Animals were always exposed to the light stimulation protocols (2 hours for 5 consecutive days) in the morning. During the stimulation, mice were allowed to move freely inside their cage with access to food and water *ad libitum*. After the stimulation, the animals received nesting material and were transferred back to the facility.

Control animals underwent the same transport and lab environment, but were only exposed to constant light, same intensity as the one used for the stimulation protocol.

Tissue preparation

All tissues were dissected 4h after the last post-drug treatment, passing the KXA half-life of 2-3 h (Zhang et al., 2018). For histological analysis, animals were quickly anesthetized with isoflurane (Zoetis, Cat#6089373) and secured to the perfusion plate. The chest was open to expose the heart. The left ventricle was cannulated and the *inferior vena cava* cut. The animals were initially perfused with 20 mL of phosphate-buffered saline (PBS) with heparin (100 mg/l, Sigma, Cat#H0878), followed by 20 mL of 4% (w/v) paraformaldehyde (PFA, Sigma, Cat#P6148) in PBS using a peristaltic pump (Behr, Cat#PLP 380, speed: 25 rpm). The animals were decapitated, the brain explanted and post-fixed in 4% (w/v) PFA/PBS for 30 minutes and overnight (16h), respectively. Then the tissues were washed in PBS and stored at 4°C with 0.025% (w/v) sodium azide (VWR, Cat#786-299). For cryoprotection, the tissue was transferred to 30% (w/v) sucrose (Sigma, Cat#84097) in PBS and incubated overnight at 4°C. To increase antibody permeability, the brain slices were frozen over dry-ice and thawed at room temperature for three cycles. Then, the brain was sliced in 100 μm coronal slices on a vibratome (Leica VT 1200S), if not otherwise indicated. For parasagittal sections, the brain was divided along the midline and the same vibratome settings were used.

Immunohistochemistry

The tissue was incubated with blocking solution containing 1% (w/v) bovine serum albumin (Sigma, Cat#A9418), 5% (v/v) Triton X-100 (Sigma, Cat#T8787), 0.5% (w/v) sodium azide (VWR, Cat#786-299), and 10% (v/v) serum (either goat, Millipore, Cat#S26, or donkey, Millipore, Cat#S30) for 1 hour at room temperature on a shaker. Afterward, the samples were immunostained with primary antibodies diluted in antibody solution containing 1% (w/v) bovine serum albumin, 5% (v/v) Triton X-100, 0.5% (v/v) sodium azide, 3% (v/v) goat or donkey serum, and incubated for 48 hours on a shaker at room temperature. The following primary antibodies were used: rabbit α-Caspase 3 (Cell Signaling, Cat#9661S, Lot 45, 1:400); rat α-CD68 (AbD Serotec, Cat#MCA1957, clone FA-11, Lot 1807, 1:250); Biotinylated Hyaluronan Binding protein (Amsbio, Cat#AMS.HKD-BC41, Lot SA, 1:150); goat α-Iba1 (Abcam, Cat#ab5076, Lot FR3288145-1, 1:250); rabbit α-Iba1 (GeneTex, Cat#GTX100042, Lot 41556, 1:750); rabbit α-MMP-9 (Abcam, Cat#ab38898, Lot GR3204084-23, 1:500); guinea pig α-parvalbumin (Synaptic Systems, Cat#195004, Lot 2505, 1:500); chicken α-parvalbumin (Novus Biologicals, Cat#NBP2-50036, Lot 72715, 1:1000); rabbit α-P2y12 (Sigma, Cat#HPA014518, Lot F119293, 1:200); chicken α-S100β (Synaptic Systems, Cat#287006, Lot 1-3, 1:500); *Wisteria floribunda* lectin – fluorescein-labeled (Szabo-Scandic, Cat#VECFL-1351, Lot ZE0611, 1:200); *Wisteria floribunda* lectin – biotinylated (Szabo-Scandic, Cat#VECB-1355, Lot ZE0424, 1:200). The slices were then washed 3 times with PBS and incubated protected from light for 2 hours at room temperature on a shaker, with the secondary antibodies diluted in antibody solution. The secondary antibodies raised in goat or donkey were purchased from Thermo Fisher Scientific (Alexa Fluor 488, Alexa Fluor 568, Alexa Fluor 647, 1:2000). The slices were washed 3 times with PBS. The nuclei were labeled with Hoechst 33342 (Thermo Fisher Scientific, Cat#H3570, 1:5000) diluted in PBS for 15 minutes. The slices were mounted on microscope glass slides (Assistant, Cat#42406020) with coverslips (Menzel-Glaser #0) using an antifade solution [10% (v/v) mowiol (Sigma, Cat#81381), 26% (v/v) glycerol (Sigma, Cat#G7757), 0.2M tris buffer pH 8, 2.5% (w/v) Dabco (Sigma, Cat#D27802)].

Confocal microscopy

Images were acquired with a Zeiss LSM880 Airyscan upright or inverted, or with a Zeiss LSM800 upright. Tile scan overview images showing the cortical area were taken using a Plan-Apochromat 10 × / NA 0.45 Air objection. To quantify image details such as number of PNN-coated cells, we used a Plan-Apochromat 40 × oil immersion objective N.A. 1.4 and acquired 2 × 2 tile scan z stacks with a resolution of 0.208 × 0.208 × 0.371 μm.

Image analysis

Confocal images were loaded in Fiji 1.52e (https://imagej.net/Fiji). To remove the background, the rolling ball radius was set to 35 pixels, and images were filtered using a median 3D-filter with x, y, z radius set at 3. Image stacks were exported as .tif files, converted to .ims files using the Imaris converter, and imported into Imaris 8.4.2. (Bitplane Imaris).

Orthogonal projection: Images were created with the "Section" tool in Imaris 9.3.1. A cell-of-interest was cropped out from the 40x 2x2 tile scan image with a crop area of 50 × 50 μm. Then, the "Normal view" option was selected in the "view" bar and a single plane orthogonal projection was created. The white cross indicates the focal plane of interest, which is projected on the XY, YZ and XZ plane. For *ex-vivo* imaging in Figure 2C, we show an extended orthogonal projection with the ROI dimension of 5x5x5 μm between the yellow lines.

Image location: For the analysis of the primary somatosensory cortex and the primary visual cortex, we took the region-of-interest at the cortical layers 3 to 5 of the S1(BF) and the V1.

Perineuronal net density per mm^3: Defined PNN-staining around neurons allowed directly counting PNN-coated neuronal cell bodies in each image using the spot-detection function of Imaris. The total cell count was normalized to the entire image volume and data are represented as number of cells surrounded by perineuronal nets per mm^3.

HABP intensity measurements: In contrast to WFA, which is a defined PNN marker (Härtig et al., 1992), HABP is a major ECM component (Ueno et al., 2018a). Thus, an intensity measurement of HABP was performed. 16-bit confocal z stacks were acquired using a Zeiss LSM-800 upright with aPlan APOCHROMAT 20x/0.8 (Cat#420650-9901), WD = 0.55 mm (D = 0.17 mm). The dimension of the z- stacks, centered between S1 cortical layers III and V, was 638.9x638.9x30 um. All the samples were acquired at the same day to avoid artifacts due to fluctuation of the laser power. The mean fluorescence intensity was calculated on the entire field of view using the mean gray value analysis function of Fiji, version 1.53.

Distance between $Pvalb^+$ neurons and microglia: Five $Pvalb^+$ neurons were analyzed per animal. The image area was cropped to 60 × 60 × 50 μm and the $Pvalb^+$-neuron soma defined as a spot center for the Imaris spot function, which was then converted into a surface. Typically, the cropped image contained 1-4 surrounding microglia, which were also identified via spots but not converted into surfaces. A surface-spot distance Imaris extension was used to calculate the distance between the centers of surfaces/spots of neuronal and microglial cell bodies.

CD68, MMP-9, WFA volume within cells: Surface renderings were generated on microglia, CD68, MMP-9, and WFA/PNN z stacks using the surface rendering module of Imaris 8.4.2. Surfaces were generated with the surface detail set to 0.2 μm. To obtain CD68 or MMP-9 surface within microglia, or the surface of WFA within the microglial CD68, the surface-surface coloc plugin was used. This analysis was performed on the entire image. The total percentage of perineuronal net volume within this microglial CD68 volume was calculated per image.

% of MMP-9 puncta in cell population: The 2x2 40x confocal tile scans were visually inspected. Cells that contain at least one MMP-9 puncta inside were considered as positive. For microglia, we considered the cell body and processes. For $Pvalb^+$ neurons, we counted the cell body.

Cell density per mm^3: In each image, either $Pvalb^+$ neurons or $Iba1^+$ microglia were counted using the spot detection function of Imaris. The total cell count was normalized to the entire image volume and data are represented as number of cells per mm^3.

Adult ocular dominance plasticity

In P60-67 animals of both sexes (8 male and 8 female for saline-treated, 9 male and 9 female for KX-treated), we implanted tapered tungsten microelectrodes (300-500 MΩ) bilaterally in the binocular zone of L4 in the V1 as previously described (Fong et al., 2016; Sawtell et al., 2003). Animals recovered for at least one week from surgery before the start of KX (or saline) treatment to minimize interference of micro- and astrogliosis around the implanted electrodes. 2 days prior to recording the first visual evoked potentials (VEPs), we habituated the animals to restraint and the gray screen with binocular viewing for 30 min (first day) and monocular viewing (second day) for 15 min each eye using an opaque paddle to restrict vision to one eye per session. For VEP recordings, we exposed animals to sinusoidal gratings at 0.2 cycles per degree and 100% contrast, and phase-reversed at 2 Hz as described (Fong et al., 2016; Sawtell et al., 2003). Every day of recording we used a novel orientation stimulus with at least 30° offset from a previously shown orientation. We used custom software written in C++ and MATLAB to analyze the VEPs. Monocular deprivation (MD) was performed at P78 at 1-3 h after recording a baseline PreMD VEP. Animals were anesthetized using isoflurane (1%–3% in oxygen) and maintained on a heated surface for the whole procedure. One eye of each animal was sutured shut for 3 days using 1-2 mattress stitches of sterile Prolene 6-0 (Ethicon). At P81, all eyes were opened and rinsed with sterile eye drops under the same anesthesia conditions. PostMD recordings on that day (day 0) were performed at least 1hr after opening the eye to allow full recovery from anesthesia. For all recordings, animals were brought to the lab at least 30 min prior to the experiment.

For randomization and blind testing, we divided the animals in two groups that were randomly assigned to one investigator. Each investigator injected the assigned group and never worked with those animals again until the full experiment was done and unblinding was necessary to run statistics.

Live imaging of WFA/microglia

Adult $Cx3Cr1^{CreERT2\ het}/Ai9^{het}$ mice were briefly anesthetized with isoflurane (Zoetis) prior to decapitation. The brain was quickly removed and submerged in ice-cold pre-carbogenated artificial cerebrospinal fluid (aCSF, 125 mM NaCl, 25 mM $NaHCO_3$,

25 mM glucose, 2.5 mM KCl, 1.25 mM NaH_2PO_4, 2 mM $CaCl_2$, 1mM $MgCl_2$). The tissue was sliced at 350 μm using a Leica VT 1200S Vibratom and incubated in *Wisteria floribunda* lectin –fluorescein-labeled (Szabo-Scandic, Cat#VECFL-1351, Lot ZE0611, 1:50 dilution) for 30 mins in constantly carbogenated aCSF. One hemisphere was mounted on black filter paper (Millipore, Cat# HABP02500) which was fixed in a closed perfusion chamber (RC-30 Warner Instruments) and constantly perfused (0.3 ml/min) with carbogenated aCSF at 37°C throughout the acclimatization (1 h) and imaging acquisition periods.

Images were acquired using an Andor Dragonfly spinning disc microscope equipped with a 40 × Nikon Apochromat water objective (40 × W NA 1.15/WD 0.6 mm) and a temperature-controlled chamber (37°C). Z stacked images were captured simultaneously every minute for 30 mins using the Zyla sCMOS and iXon EMCCD cameras. A 308 × 308 μm field of view was imaged with 1024 × 1024 pixels, giving 0.301 μm/pixel in XY and a Z-step size of 0.4 μm. The same exposure time (50 ms) and electron multiplying gain settings (200 for EMCCD) were applied to all imaging sessions. Drifting was corrected using the translational and rotational drifting correction option of the Imaris tracking spot function.

In-vivo electrophysiology

Surgery: C57BL/6J adult males were anesthetized with isoflurane (5% induction, 2.5% maintenance) in 0.6 l/min O_2 and were kept at 37°C using a heating pad connected to a rectal probe during the surgical procedure. After fixing the animal to a stereotaxic apparatus (KOPF digital plus) and septic sterilization, the skin over the skull was cut. The exposed skull was treated with 3% (v/v) H_2O_2 (Sigma, Cat#216763) in PBS to remove the periosteum and to ensure enhanced cement adhesion.

The craniotomy (Ø ≈2 mm) was performed with a micro drill centered at Bregma −3.4 and interaural 2.5 mm. These stereotaxic coordinates for the primary visual cortex were calculated on the Paxinos mouse brain atlas.

To record LFPs though the entire cortical layers, a 2-shank-32-channel chronic silicone probe (Cambridge Neurotech L2 sharp), equipped with an Omnetics 32 connector, was inserted into the brain parenchyma. The probe was grounded on both cerebellar hemispheres using two bone screws (FST, Cat#19010-00). The skull was then covered with dental cement (Henry Schein, NX3, Cat#246367). The pain was controlled with Metamizol (Sanofi Aventis, Cat#Ay005, *s.c.* 200 mg/kg during surgery) and with Meloxicam (Boehringer-Ingelheim, Cat#KPOEH3R, *s.c.* 5 mg/kg after surgery every 24 h for 3 consecutive days). The animals recovered at least for 2 weeks before used for experiments and did not develop any signs of seizures.

Recording: All recordings were performed in the morning (animal light phase). On the day of the experiment, the animal was connected to the head-stage, and neuronal activity during the light flickering protocol was recorded using an Intan RHD USB interface board with a sampling rate of 30 kHz for 10 minutes.

Data analysis: was performed with Python (Version 3.7), MATLAB R2019b, and MatPlotLib (Version 3.4.1) Local field potentials (LFPs) were extracted from the *in-vivo* recordings using a 3rd-order low-pass Butterworth filter with a cut-off frequency of 300Hz, and were further downsampled to 3 kHz. A multi-tapering approach, as implemented in the Chronux toolbox (Version 2.12), was used to calculate the power spectra. Periodograms were estimated using 5 Slepian sequences with time-bandwidth product of 3 with zero-padding on the fast Fourier transforms. Periodograms were normalized over the total power from 0.5 to 100 Hz.

QUANTIFICATION AND STATISTICAL ANALYSIS

All statistics were performed using R (version 3.4.4), if not otherwise indicated. Models were generated by changing the default contrast for unordered variables to "contr.sum." This allows type III ANOVA to be applied to the model to evaluate the overall contribution of unordered effects on the response variable. Reported *P* values of post hoc tests performed via the "multcomp" package (Hothorn et al., 2008) were corrected for multiple testing according to the default single-step method. If not otherwise indicated, all possible pairwise comparisons were performed. Linear regression was performed using the lme4 package (version 1.1-17) (Bates et al., 2015). Analyzed results were exported from Imaris into an Excel file, which was loaded into R via the xlsx package (version 0.6.1) (Dragulescu, 2014). Plots were generated using ggplot2 (version 3.0.0) (Wickham, 2016). All error bars in the manuscript represent standard error of the mean (SEM), calculated with mean_se() as part of the hmisc package in ggplot2. A short description of each test and the results can be found in the figure legends. Details about the statistical models as well as the results of the statistical analysis for each figure are found in the Table S1. * $p < 0.05$, ** $p < 0.01$, *** $p < 0.001$, ^{ns} $p > 0.05$.

Combined controls

To compare experimental groups subjected to different injection paradigms, we first compared controls that received 1 × , 3 × , or 6 × saline injections and obtained a mean value from the means of these conditions (control), which served as the control for further statistical testing.

Perineuronal net density per mm^3

Each data point represents the count of neurons surrounded by PNNs in one image per animal (biological replicates). We calculated cell densities as a percentage, with the respective control set to 100%. We used linear regression to predict cell density per mm^3 (as absolute values or as percentages compared to the respective control) by experimental condition in cases where more than two levels were involved. We used a two-sided t test to investigate differences between experimental conditions in cases where only two levels were involved. In this case, *P* values were adjusted using the "p.adjust" function and the method set to "BH."

Sex differences

To compare removal and recovery of perineuronal nets between the sexes, we tested for differences between males and females within each experimental group using linear regression, and selected post hoc contrasts for the desired comparisons. Models are described in Table S1 (Models, A).

Ocular dominance plasticity experiments statistics: To determine sample size, we ran a pilot experiment with 5 animals injected with 3 × KX and the same timeline as the final dataset. We considered the subject and the properties of each time point (contralateral/ipsilateral ratio) to make the simulation using R. We simulated that the control (saline) group did not change over time, i.e., the mean value remained the same, with the given SD by the real data at baseline. We simulated that the treated group could change similar to the real data but with higher number of mice. The pilot data showed values decreasing compared to the baseline, with negative coefficients calculated using a linear model. We then performed 1000 simulations for 5, 10, 20, 40, 50 mice per group, and we calculated the two-way ANOVA for repeated-measures statistics and *P* value. We checked whether any difference (*P* value < 0.05) was detected between groups and between group:time interactions in every simulation. The results showed that we needed between 12 and 20 animals to observe $> 80\%$ power. The final dataset included 18 ketamine-treated and 16 saline-treated animals. We did not include the animals from the pilot experiment as that experiment was not performed blind to treatment.

We used Prism 8 to run statistical analyses and generate graphs on the final dataset. To analyze the contra/ipsi ratio (Figure 1G) we performed a two-way repeated-measures ANOVA to examine changes over time and across treatment conditions. We then ran a Dunnett's multiple comparisons test to compare changes of baseline values over time. To analyze the VEP magnitude (Figures 1H and 1I), we ran a one-way repeated-measures ANOVA after determining that the data were normally distributed (using the Shapiro-Wilk test) on ipsilateral responses in the saline group. For the contralateral saline-treated group and both the contralateral and ipsilateral ketamine-treated groups, the normality test showed that the data was not normally distributed and we therefore ran a Friedman test. If a significant effect ($p < 0.05$) was found, we then performed a multiple comparisons test using Dunnett's correction.

MMP volume within cells: The total percentage of MMP volume within cell volume per image was calculated. A two-sided t test was performed, and *P* values were adjusted using the "p.adjust" function and the method set to "BH" (Table S1, Models, B).

Distance between Pvalb$^+$ neurons and microglia. The exported Imaris file contained the minimal distance values from five analyzed images per animal. We used linear regression to predict the minimal distance per experiment condition. Models are described in Table S1 (Models, C). A random effect was included to account for individual animals and the fact that their technical replicates were not independent.

PNN volume within microglial CD68: Each data point represented several microglia within one image per animal (biological replicates). We used linear regression to predict the percentage of PNN volume within microglial CD68 volume under experimental conditions. For the CD68 volume within microglia, we used linear regression to predict the percentage of CD68 volume within the microglia volume under experimental conditions. Models are described in Table S1 (Models, D).

PNN volume within microglia in ex-vivo *imaging*: We used linear regression to predict the square root-transformed percentage of PNN volume within the microglia volume under experimental conditions (Table S1, Models, A). To account for repeated-measurements, we included an identifier for individual animals as a random factor.

Cell density per mm^3: Each data point represented neurons stained for parvalbumin or microglia stained for Iba1 within one image per animal (biological replicates). We used a two-sided t test to investigate differences between experimental conditions in cases where only two levels were involved. *P* values were adjusted with the "p.adjust" function and the method set to "BH."

To evaluate the efficiency of microglial depletion via PLX in treated (PLX_kxa_3x) as well as saline-injected (PLX_ctrlsal_3x) animals, we compared their microglial density with saline-injected animals that were not exposed to PLX (ctrlsal_3x). For this, we calculated the percentage with the no-PLX group set to 100%. We used linear regression to predict the percentage compared to the control under experimental conditions. Models are described in Table S1 (Models, E).

Cell Reports, Volume *36*

Supplemental information

Microglia enable mature perineuronal nets disassembly upon anesthetic ketamine exposure or 60-Hz light entrainment in the healthy brain

Alessandro Venturino, Rouven Schulz, Héctor De Jesús-Cortés, Margaret E. Maes, Bálint Nagy, Francis Reilly-Andújar, Gloria Colombo, Ryan John A. Cubero, Florianne E. Schoot Uiterkamp, Mark F. Bear, and Sandra Siegert

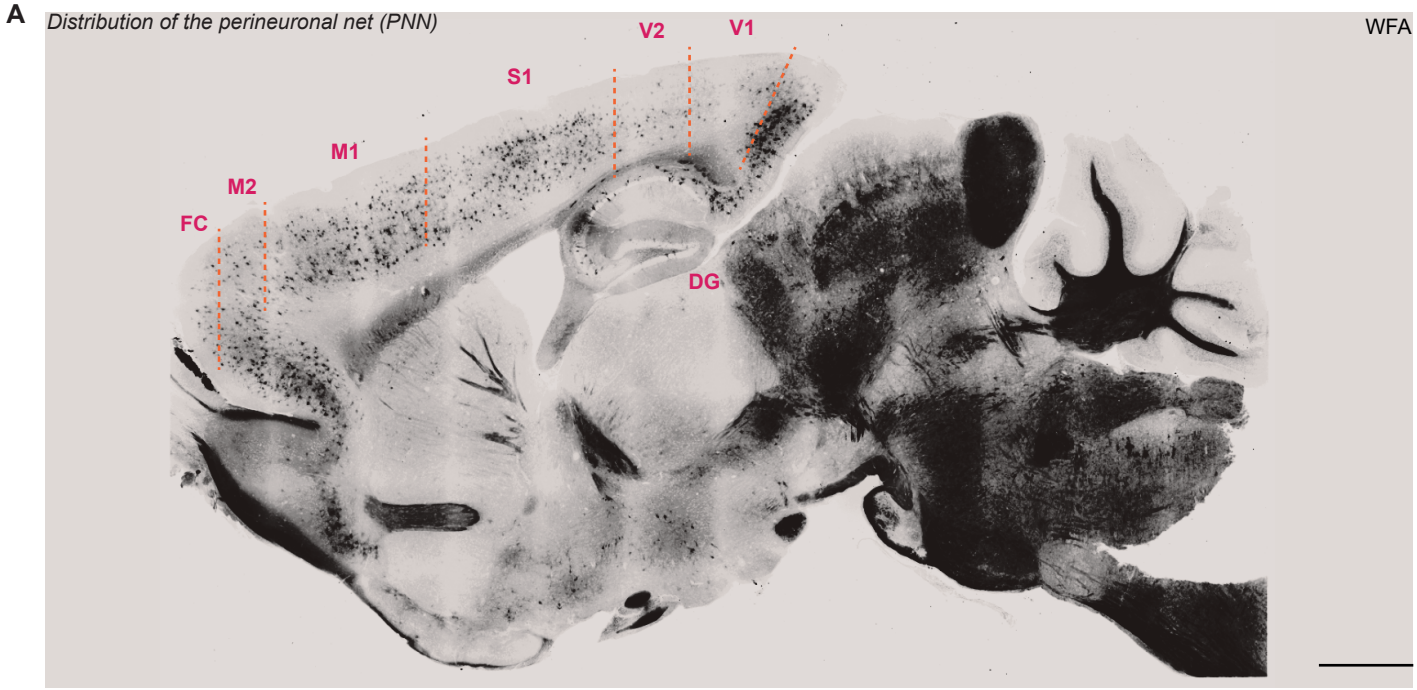
A
Distribution of the perineuronal net (PNN)
WFA
V2
V1
S1
M1
M2
FC
DG

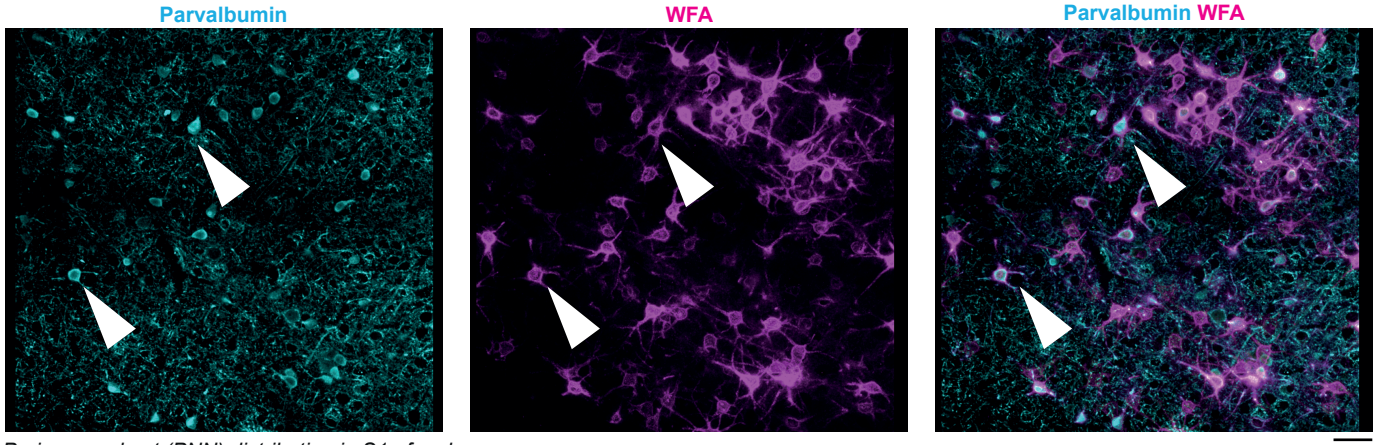
B
PNN surrounding a subpopulation of parvalbumin⁺ interneurons in the primary somatosensory cortex 1 (S1)
Parvalbumin
WFA
Parvalbumin WFA

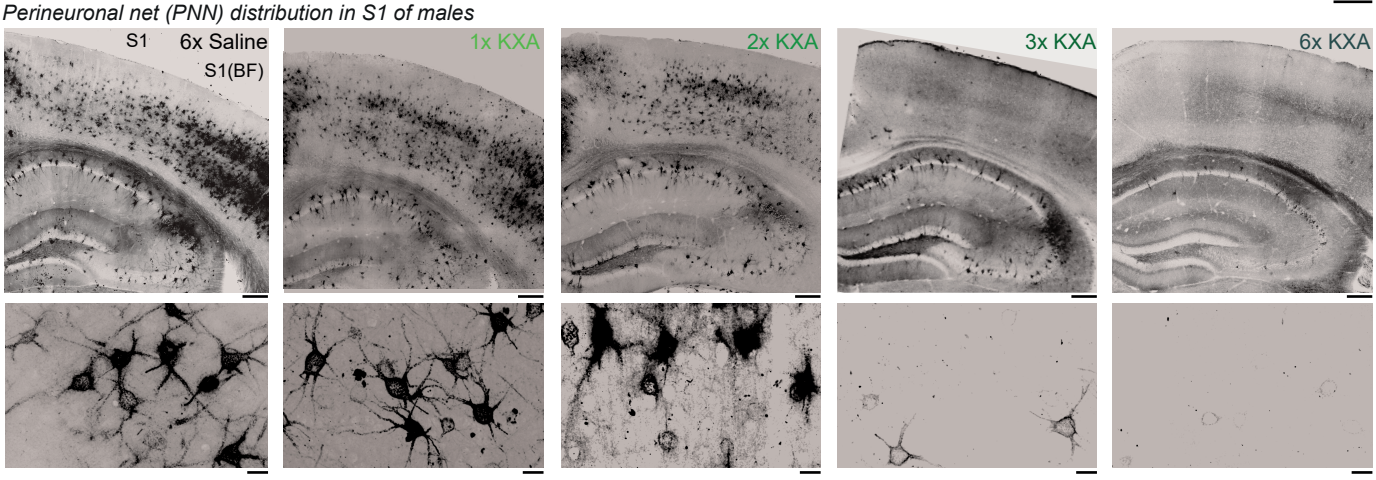
C
Perineuronal net (PNN) distribution in S1 of males
S1
6x Saline
S1(BF)
1x KXA
2x KXA
3x KXA
6x KXA

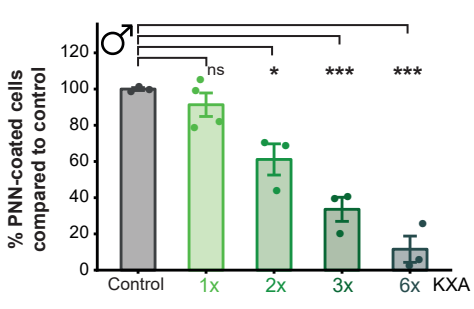
D
Density of PNN-coated cells
% PNN-coated cells compared to control
ns
*
***
***
Control
1x
2x
3x
6x
KXA

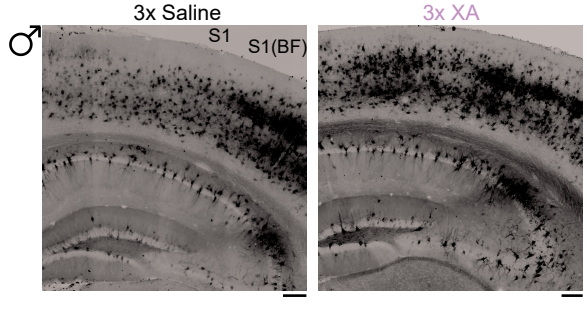
E
PNN distribution under xylazine-acepromazine (XA) alone
3x Saline
3x XA
S1
S1(BF)

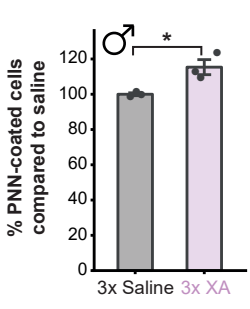
F
Density of PNN-coated cells
% PNN-coated cells compared to saline
*
3x Saline
3x XA

Figure S1. PNN distribution in the cortex. Related to Figure 1.

(A) Parasagittal brain section of an 8-week-old male immunostained with WFA (*Wisteria floribunda* agglutinin). Scale bar: 1000 µm. (B) Image into primary somatosensory cortex (S1) showing parvalbumin-positive interneurons (cyan) surrounded by WFA (magenta). Arrow: WFA-coated parvalbumin^{+} cell. Scale bar: 300 µm. DG, hippocampal dentate gyrus. FC, frontal cortex. M1, primary motor cortex 1. M2, secondary motor cortex 2. V1, primary visual cortex. V2, secondary visual cortex. (C-F) Effects of 6× saline, 1×, 2×, 3×, or 6× KXA injections in males. Females, see **Figure 1B-1E**. (C) Coronal brain sections immunostained for WFA with zoom-in into S1. Scale bar: 200 µm, zoom-in: 20 µm. (D) Percent mean change of WFA-coated cells ± SEM compared to control for males as quantified from separately taken 2x2 higher magnification images. Linear regression model: $P_{♂} < .0001$ with selected post-hoc comparisons. (E) Immunostaining for WFA after 3× saline or XA exposure. Scale bar: 200 µm. (F) Percent mean change ± SEM of WFA-coated cells for 3× saline and xylazine-acepromazine (XA) as quantified from separately taken 2x2 higher magnification images. Two sample t-test: $P_{♂} = 0.0481$. KXA, ketamine-xylazine-acepromazine. PNN, perineuronal net. S1(BF), somatosensory 1, barrel field. SEM, standard error of the mean. Each dot represents one animal (3-5 animals per condition with exception of the control in (D), which shows the mean value of all controls. Ssee also **Figure S2B**). SEM, standard error of the mean. $*P < .05$, $***P < .001$. $^{ns}P > .05$.

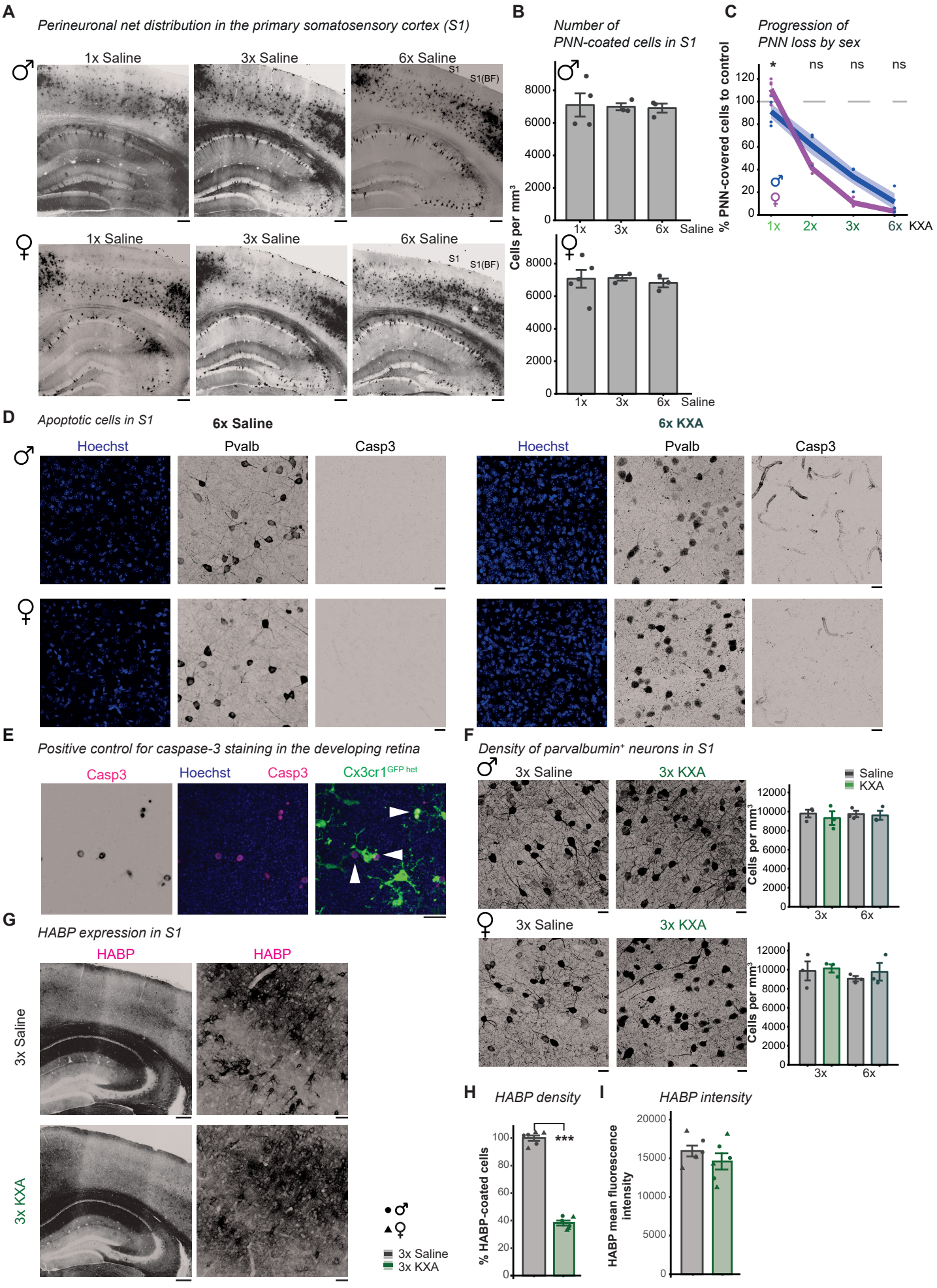
A
Perineuronal net distribution in the primary somatosensory cortex (S1)
1x Saline
3x Saline
6x Saline
S1
S1(BF)
B
Number of PNN-coated cells in S1
Cells per mm³
Saline
C
Progression of PNN loss by sex
% PNN-covered cells to control
ns
KXA
D
Apoptotic cells in S1
6x Saline
6x KXA
Hoechst
Pvalb
Casp3
E
Positive control for caspase-3 staining in the developing retina
Cx3cr1GFP het
F
Density of parvalbumin⁺ neurons in S1
3x Saline
3x KXA
G
HABP expression in S1
HABP
H
HABP density
% HABP-coated cells
I
HABP intensity
HABP mean fluorescence intensity

Figure S2. No PNN loss upon repeated saline injection, and no ketamine-induced apoptosis. Related to Figure 1.

(A) Coronal brain sections immunostained for WFA (*Wisteria floribunda* agglutinin) for 1×, 3×, or 6× saline injections in males (top) and females (bottom). Scale bar: 200 µm. (B) Mean number of WFA-coated cells ± SEM after 1×, 3×, 6× saline injections. Each dot represents one animal. Linear regression model: $P_{♂}$= 0.9670. $P_{♀}$= 0.9017. (C) Progression of PNN loss for each sex after ketamine treatment. Linear regression model: $P < .0001$ with post-hoc comparison. (D) Immunostaining for parvalbumin (Pvalb) or caspase (Casp3) and Hoechst (blue) for 6× saline or KXA injection in S1. Casp3 staining in 6× KXA shows background blood vessel staining. Scale bar: 20 µm. (E) Positive control for Casp3 staining in a retina of $Cx3Cr1^{GFP\ het}$ 10 days postnatal. Arrow: microglia engulfing $Casp3^{+}$ nuclei. Scale bar: 20 µm. (F) Immunostaining for $Pvalb^{+}$ neurons treated with 3× saline or KXA in S1. Scale bar: 20 µm. Bar chart represents $Pvalb^{+}$ neuron mean density ± SEM after 3× or 6× injections. Linear regression model: $P_{♂}$= 0.9037. $P_{♀}$= 0.7565. Each dot represents an animal (3-5 animals per condition. (G) Coronal brain sections immunostained for hyaluronic acid binding protein (HABP) after 3× saline or 3× KXA injections with zoom-in into S1 at cortical layer 3-5. Scale bar: 200 µm, zoom-in: 50 µm. (H-I) Percent mean change ± SEM of HABP-coated cells compared to saline control (H) and mean fluorescence intensity (I) compared to saline control as quantified by separate taken 2x2 higher magnification images. Two sample t-test: (H) $P < .0001$. (I) $P = 0.312$. KXA, ketamine-xylazine-acepromazine. PNN, perineuronal net. S1, primary somatosensory cortex. S1(BF), somatosensory 1, barrel field. SEM, standard error of the mean. $*P < .05$, $***P < .001$, $^{ns}P > .05$.

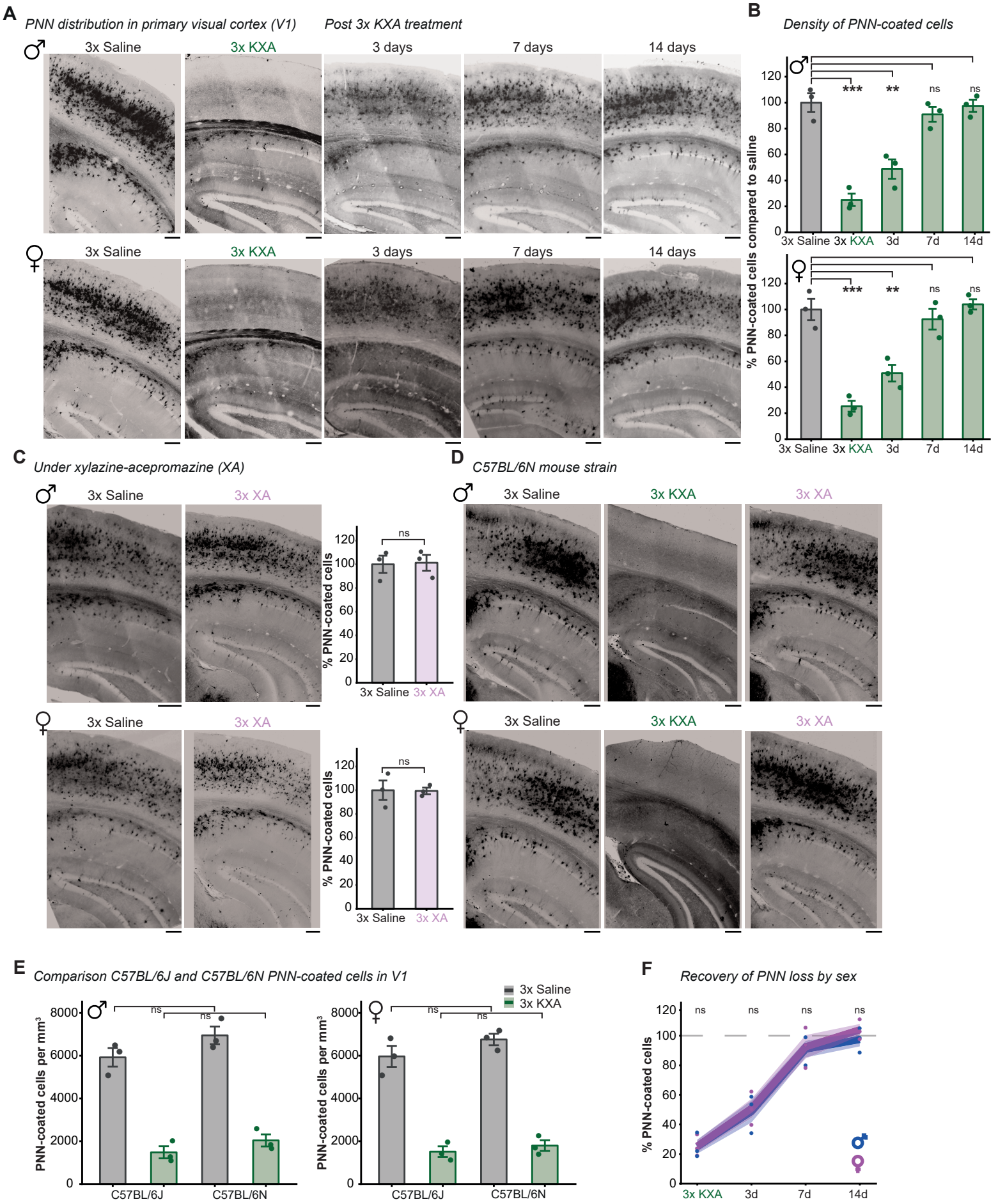
A
PNN distribution in primary visual cortex (V1)
Post 3x KXA treatment
3x Saline
3x KXA
3 days
7 days
14 days
B
Density of PNN-coated cells
% PNN-coated cells compared to saline
***
**
ns
3x Saline
3x KXA
3d
7d
14d
C
Under xylazine-acepromazine (XA)
3x XA
% PNN-coated cells
D
C57BL/6N mouse strain
E
Comparison C57BL/6J and C57BL/6N PNN-coated cells in V1
PNN-coated cells per mm³
C57BL/6J
C57BL/6N
F
Recovery of PNN loss by sex

Figure S3. Ketamine causes transient PNN loss in V1, and is independent from repeated xylazine-acepromazine treatment alone and mouse strain background. Related to Figure 1. (A) Coronal brain sections immunostained for WFA (*Wisteria floribunda* agglutinin) after 3× saline or 3× KXA and 3, 7, and 14 days after last injection for 3× KXA in males (top) and females (bottom). Scale bar: 200 µm. (B) Percent mean change ± SEM of PNN-coated cells compared to saline-treated animals as quantified by separate taken 2x2 higher magnification images. Linear regression model: $P_{♂} < .0001$ and $P_{♀} < .0001$ with selected post-hoc comparisons. (C-D) Coronal brain sections for males (top) and females (bottom) immunostained for WFA after 3× saline or xylazine-acepromazine (XA) injection in C57BL/6J (C) or C57BL/6N (D). Scale bar: 200 µm. (C) Mean percent of WFA-coated cells ± SEM. Two sample t-test: $P_{♂} = 0.8991$. $P_{♀} = 0.9516$. (E) Mean percent of PNN-coated cells ± SEM of C56BL/6J and C56BL/6N mouse strains for males (left) and females (right) as determined by separate 2x2 higher magnification images. Linear regression model: $P_{♂} < .0001$. $P_{♀} < .0001$ with selected post-hoc comparisons. (F) Recovery from PNN loss after 3× KXA in days for each sex. Linear regression model: $P < .0001$ with shown post-hoc comparison. In all bar charts, each dot represents an animal. KXA, ketamine-xylazine-acepromazine. PNN, perineuronal net. SEM, standard error of the mean. V1, primary visual cortex. $^{**}P < .01$, $^{***}P < .001$. $^{ns}P > .05$.

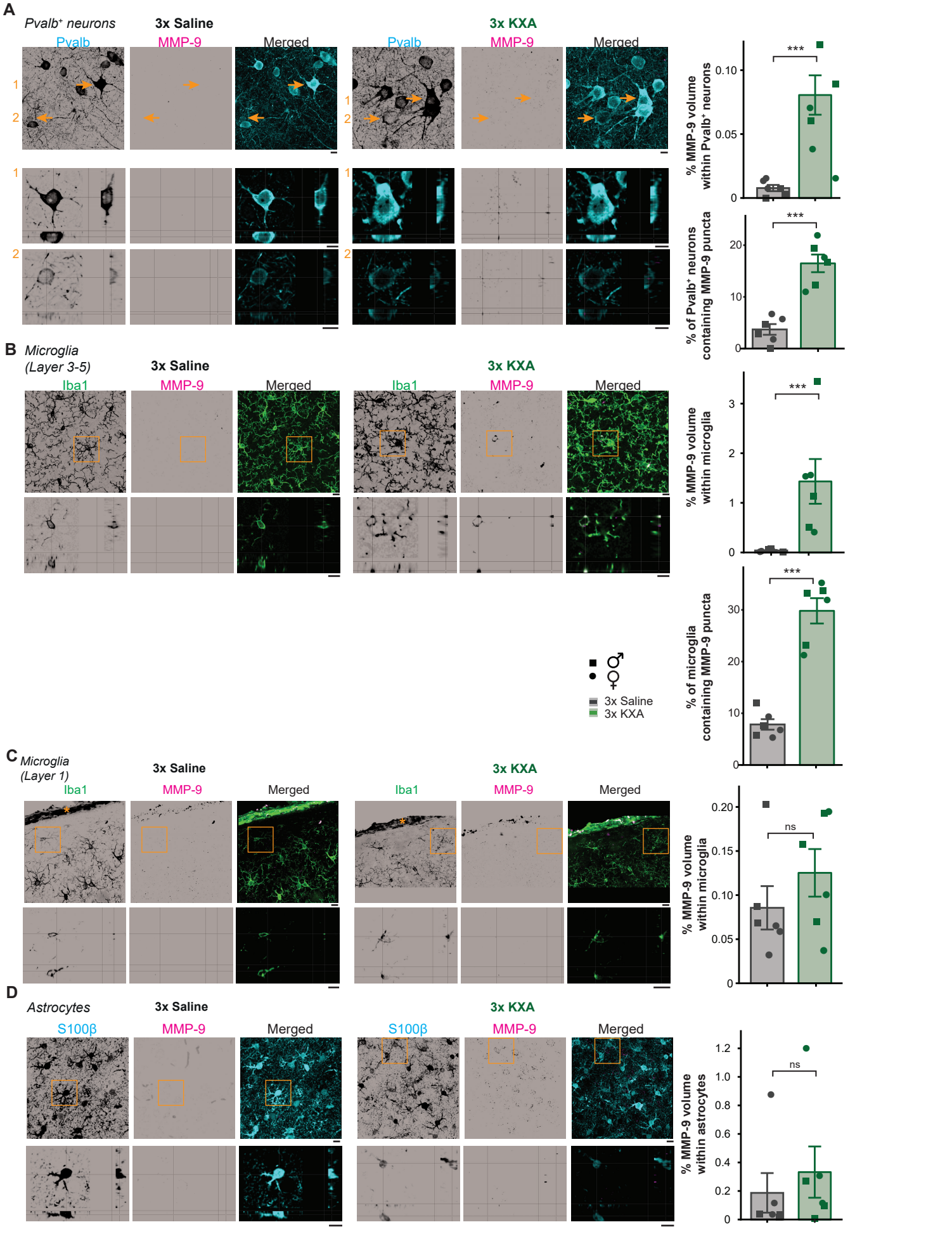
A
Pvalb⁺ neurons
3x Saline
3x KXA
Pvalb
MMP-9
Merged
% MMP-9 volume within Pvalb⁺ neurons
% of Pvalb⁺ neurons containing MMP-9 puncta
B
Microglia (Layer 3-5)
Iba1
% MMP-9 volume within microglia
% of microglia containing MMP-9 puncta
3x Saline
3x KXA
C
Microglia (Layer 1)
% MMP-9 volume within microglia
ns
D
Astrocytes
S100β
% MMP-9 volume within astrocytes
***

Figure S4. Repeated KXA treatment increased matrix-metalloproteinase-9 (MMP-9) level in Pvalb^{+} neurons and microglia located in cortical layers 3-5. Related to Figure 2.
Representative images showing immunostaining for matrix metalloproteinase-9 (MMP-9, magenta), (A) parvalbumin neurons (Pvalb, cyan), (D) astrocytes (S100β, cyan), (B) microglia in cortical layer 3-5 and (C) layer 1 (Iba1, green, *, non-parenchymal, meningeal macrophages) after 3× saline or KXA in primary somatosensory cortex. Scale bar: 10 µm. Below, zoom-in to selected cells for single plane orthogonal projection. Scale bar: 10 µm. Next, mean percent of MMP-9 volume ± SEM and for (A-B) % cells of containing MMP-9 puncta ± SEM. Two sample t-test: (A) Pvalb^{+} neurons, $P < .0001$. Below: $P < .0001$. (B) Microglia in cortical layer 3-5, $P < .0001$. Below: $P < .0001$. (C) Microglia in cortical layer 1, $P = 0.4080$. (D) Astrocytes, $P = 0.4205$. Each dot represents one animal. KXA, ketamine-xylazine-acepromazine. ***$P < .001$, $^{ns}P > .05$.

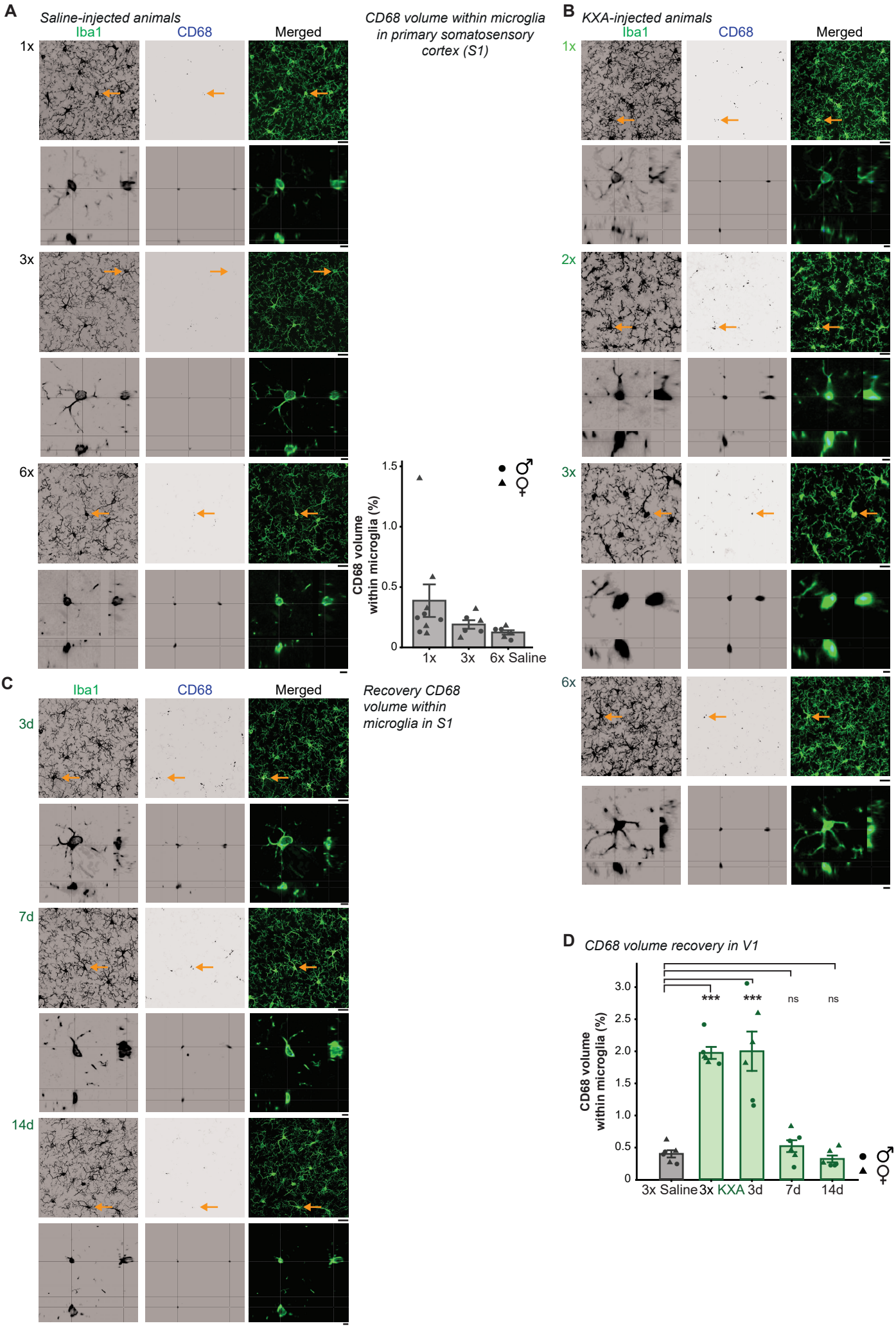
A
Saline-injected animals
Iba1
CD68
Merged
1x
3x
6x
CD68 volume within microglia in primary somatosensory cortex (S1)
CD68 volume within microglia (%)
1.5
1.0
0.5
0
1x
3x
6x Saline
B
KXA-injected animals
Iba1
CD68
Merged
1x
2x
3x
6x
C
Iba1
CD68
Merged
3d
7d
14d
Recovery CD68 volume within microglia in S1
D
CD68 volume recovery in V1
CD68 volume within microglia (%)
3.0
2.5
2.0
1.5
1.0
0.5
0
***
***
ns
ns
3x Saline
3x KXA 3d
7d
14d

Figure S5. CD68 expression increased during ketamine exposure and gradually recovered after the last injection. Related to Figure 2.

(A-C) Overview images of primary somatosensory cortex (S1) immunostained for CD68 (blue or magenta) and Iba1 (green) after repeated saline (A), KXA (B), and 3, 7, 14 days after 3× KXA injection (C). Scale bar: 20 µm. Arrow: Selected cell for zoom-in and single plane orthogonal projections below each maximum intensity projection image. Scale bar: 5 µm. (A) Mean CD68 volume within microglia ± SEM in S1. Linear regression model: $P > .05$. (D) Similar CD68-recovery in primary visual cortex (V1) as for S1 (see also **Figure 2F**). Mean percentage ± SEM CD68 volume recovery within microglia after 3× KXA injection. Linear regression model: $P < .0001$ with selected post-hoc comparisons. KXA, ketamine-xylazine-acepromazine. Each dot represents an animal. SEM, standard error of the mean. $^{***}P < .001$. $^{ns}P > .05$.

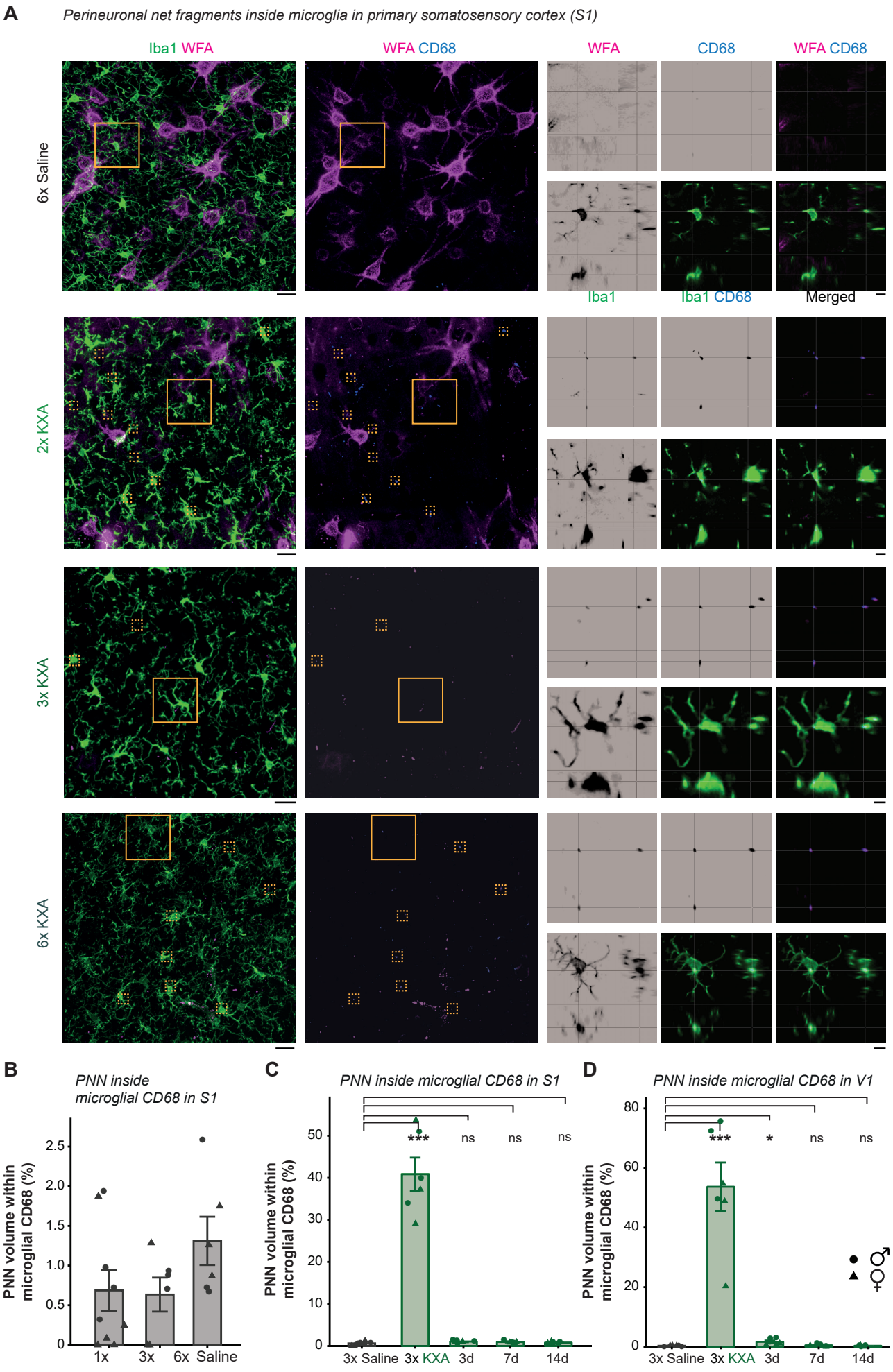
A
Perineuronal net fragments inside microglia in primary somatosensory cortex (S1)
Iba1 WFA
WFA CD68
WFA
CD68
WFA CD68
Iba1
Iba1 CD68
Merged
6x Saline
2x KXA
3x KXA
6x KXA
B
PNN inside microglial CD68 in S1
PNN volume within microglial CD68 (%)
1x
3x
6x
Saline
C
PNN inside microglial CD68 in S1
PNN volume within microglial CD68 (%)
***
ns
ns
ns
3x Saline
3x KXA
3d
7d
14d
D
PNN inside microglial CD68 in V1
PNN volume within microglial CD68 (%)
***
*
ns
ns
3x Saline
3x KXA
3d
7d
14d

Figure S6. Multiple microglia contain PNN/CD68 fragments after ketamine exposure. Related to Figure 2.

(A) Overview images of female primary somatosensory cortex (S1) immunostained for PNN (WFA, magenta), microglia (Iba1, green), and endosomal-lysosomal marker CD68 (blue) after 6× saline, 2, 3, 6× KXA. Dashed frames: CD68/WFA colocalizations within field of view. Scale bar: 30 µm. Frame indicates cell selected for zoom-in and single plane orthogonal projections. Scale bar: 10 µm. (B-D) Percentage of mean WFA volume within microglial CD68 ± SEM in animals treated with 1×, 3× or 6× saline (B), after recovery from 3× KXA (C) in S1 and (D) primary visual cortex (V1). Linear regression model: (C) $P = 0.179$. (D) $P < .0001$. (E) $P < .0001$ with selected post-hoc comparisons. Each dot represents an animal. KXA, ketamine-xylazine-acepromazine. PNN, perineuronal net. SEM, standard error of the mean. *$P < .05$, ***$P < .001$, $^{ns}P > .05$.

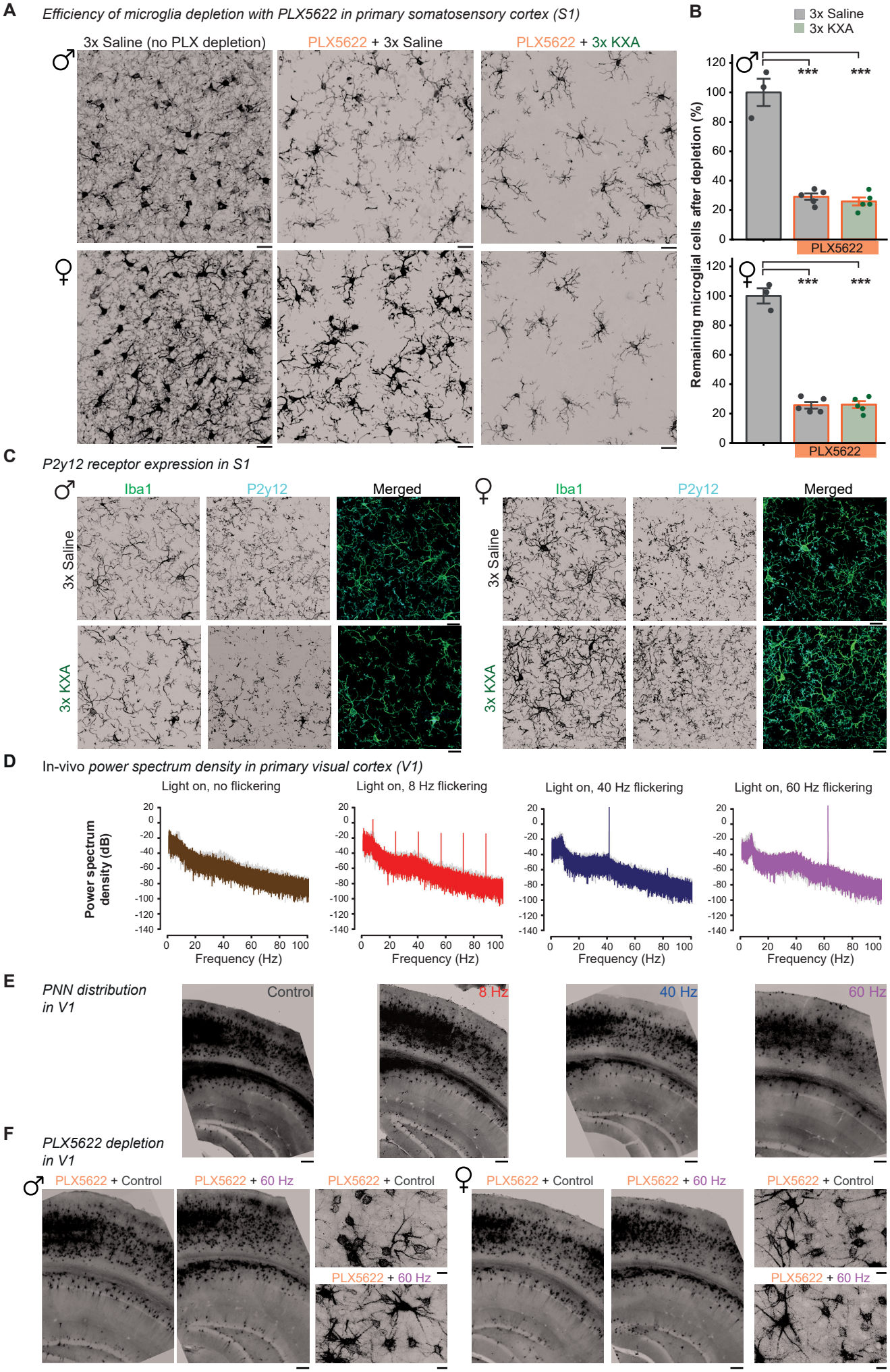
A
Efficiency of microglia depletion with PLX5622 in primary somatosensory cortex (S1)
3x Saline (no PLX depletion)
PLX5622 + 3x Saline
PLX5622 + 3x KXA
B
3x Saline
3x KXA
Remaining microglial cells after depletion (%)
***
***
PLX5622
C
P2y12 receptor expression in S1
Iba1
P2y12
Merged
3x Saline
3x KXA
D
In-vivo power spectrum density in primary visual cortex (V1)
Light on, no flickering
Light on, 8 Hz flickering
Light on, 40 Hz flickering
Light on, 60 Hz flickering
Power spectrum density (dB)
Frequency (Hz)
E
PNN distribution in V1
Control
8 Hz
40 Hz
60 Hz
F
PLX5622 depletion in V1
PLX5622 + Control
PLX5622 + 60 Hz

Figure S7. Consequences of microglial manipulation. Related to Figures 3 and 4.
(A-B) Efficiency of microglia depletion with PLX5622. (A) Representative images of coronal brain sections immunostained for Iba1 (microglia) in primary somatosensory cortex (S1). Mice treated for 1.5 weeks with PLX5622 prior to the start of 3× injections (as outlined in **Figure 3A**). Scale bar: 20 µm. (B) PLX5622 depletion efficiency. Remaining mean number of microglia as a percentage of control (3× saline) ± SEM. Each dot represents an animal. Linear regression model: $P_{♂} < .0001$ and $P_{♀} < .0001$ with selected post-hoc comparisons. (C) Level of microglial homeostatic marker P2Y12 does not change. Representative images of coronal brain sections immunostained for P2Y12 receptor and microglia (Iba1) treated with 3× saline or 3× KXA. Scale bar: 15 µm. (D-F) Effects of light flickering on PNN. (D) Power spectrum density plots of local field potentials across V1 cortical layers during light stimulation paradigms for no light (grey trace in the background), after light turned on and 8, 40, 60 Hz-flickering. (E-F) Representative overview images of coronal brain sections immunostained for WFA for (E) constant light, 8 Hz, 40 Hz, 60 Hz, and (F) after 1.5 weeks of PLX5622 microglia-depletion and control light and 60 Hz flickering stimulation as **Figure 4A**. Scale bar: 200 µm. KXA, ketamine-xylazine-acepromazine. SEM, standard error of the mean. ***$P < .001$.

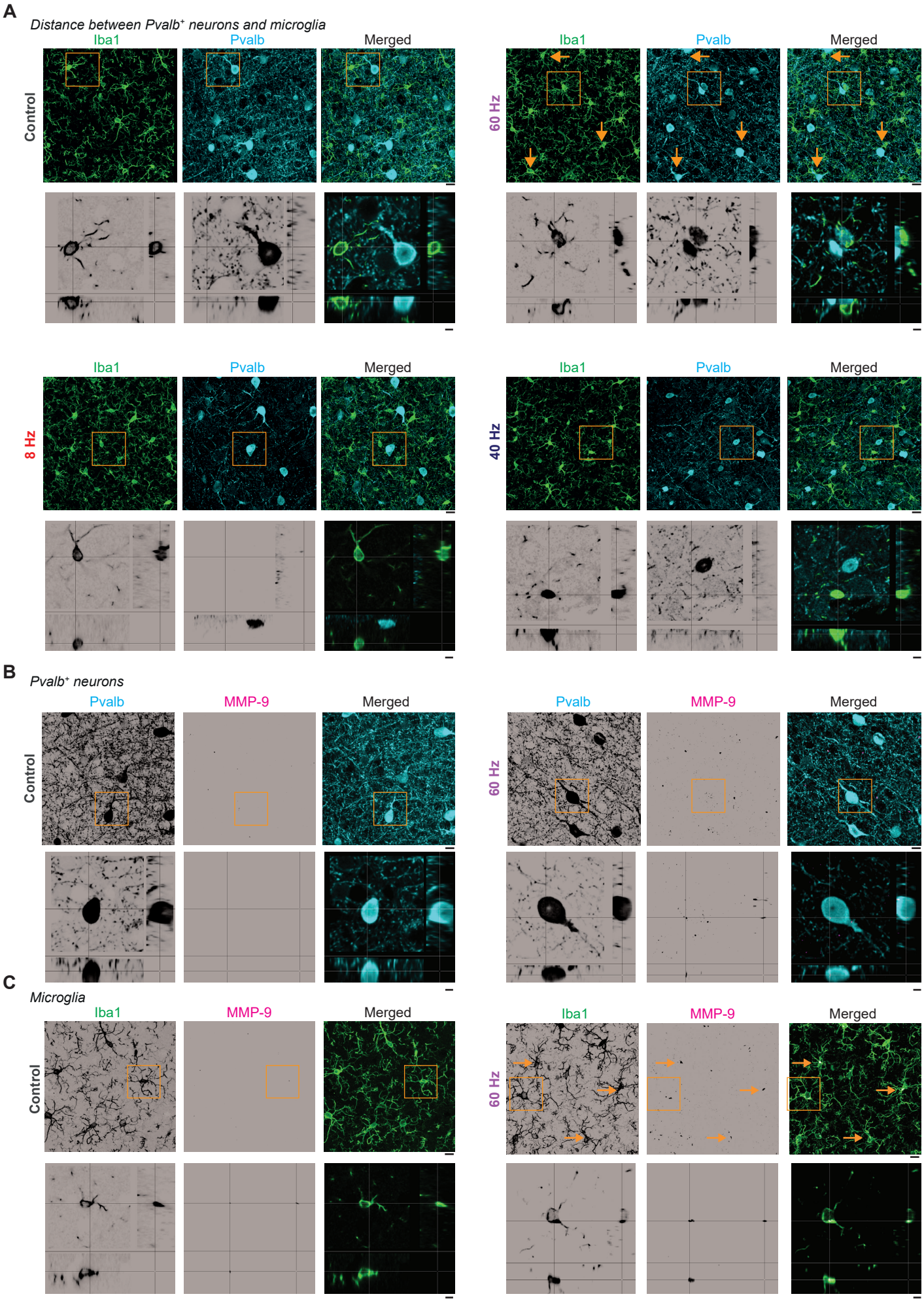
A
Distance between Pvalb+ neurons and microglia
Iba1
Pvalb
Merged
Control
60 Hz
8 Hz
40 Hz
B
Pvalb+ neurons
Pvalb
MMP-9
Merged
Control
60 Hz
C
Microglia
Iba1
MMP-9
Merged
Control
60 Hz

Figure S8. Effects of light flickering on parvalbumin$^+$ neuron-microglia distance and MMP-9 expression level. Related to Figure 4.

Representative images showing immunostaining for microglia (Iba1, green), parvalbumin (Pvalb, cyan), and MMP-9 (magenta) after (A) control light (top left), 60 Hz light flickering (top right), 8 Hz (bottom left) and 40 Hz (bottom right) in primary visual cortex (V1). Arrow: microglia in close distance of Pvalb$^+$ neurons. (B-C) MMP-9 localization within (B) Pvalb$^+$ neurons and (C) microglia. Scale bar: 10 µm. Frame indicates position of selected cell for zoom-in and single cell orthogonal projection. Scale bar: 4 µm.

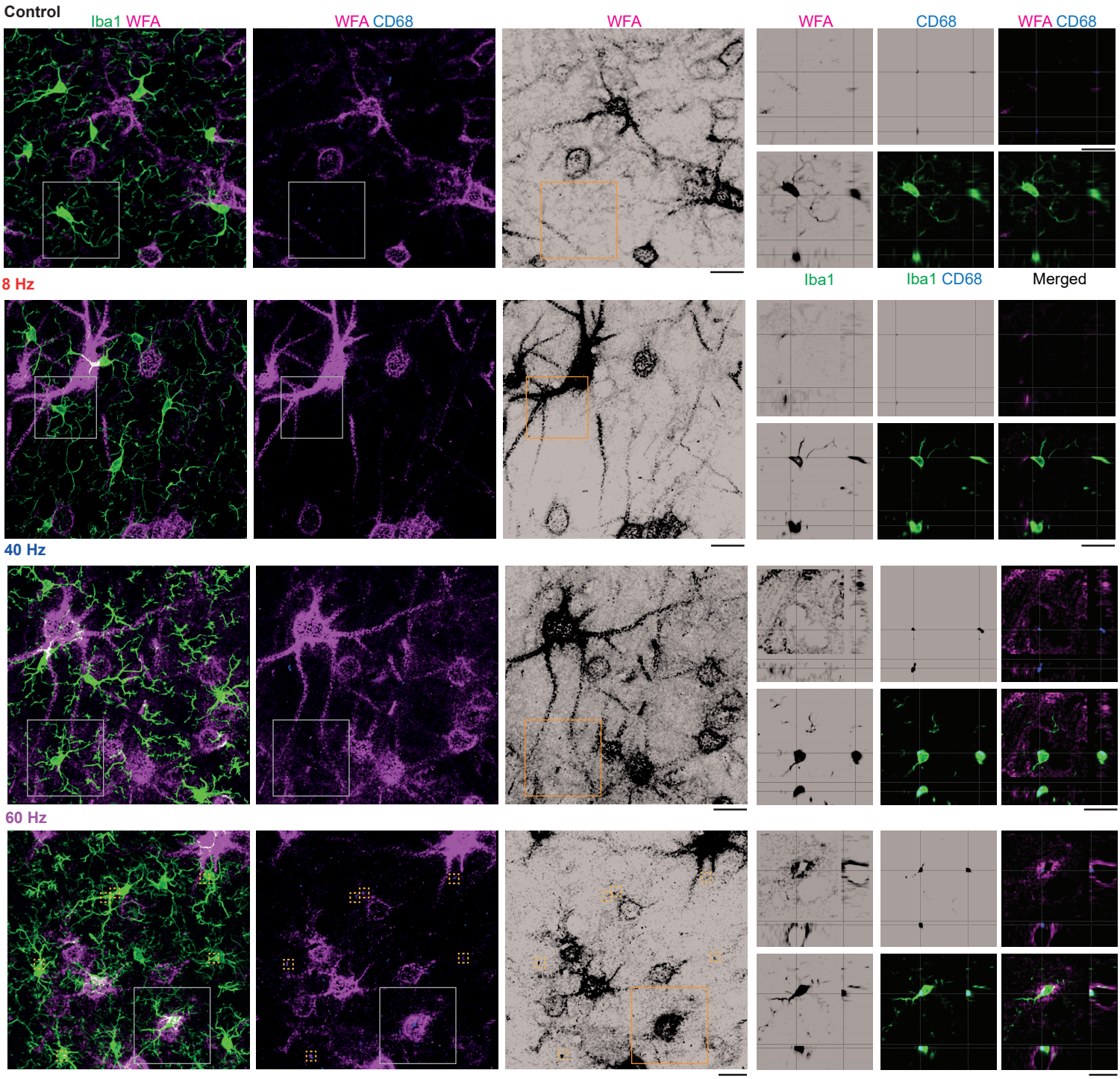
Control
Iba1 WFA
WFA CD68
WFA
WFA
CD68
WFA CD68
8 Hz
Iba1
Iba1 CD68
Merged
40 Hz
60 Hz

Figure S9. 60 Hz light-flickering induces PNN removal via microglia. Related to Figure 4. Representative overview images showing immunostaining for PNN (WFA, magenta), microglia (Iba1, green), and endosomal-lysosomal marker CD68 (blue) in primary visual cortex (V1) after constant light (control), 8 Hz, 40 Hz, or 60 Hz light-flickering stimulation. Frame indicates position of selected cell for zoom-in and single cell orthogonal projection. Scale bar: 20 µm.